Searching for Quadruply Lensed Quasars in Large Imaging Surveys

A Thesis

submitted to

Indian Institute of Science Education and Research Pune

in partial fulfillment of the requirements for the

BS-MS Dual Degree Programme

by

Arjun Murlidhar

Indian Institute of Science Education and Research Pune

Dr. Homi Bhabha Road,

Pashan, Pune 411008, INDIA.

April, 2023

Supervisors: Dr. Anupreeta More and Prof. Somak Raychaudhury

© Arjun Murlidhar 2023

Certificate

This is to certify that this dissertation entitled **Searching for Quadruply Lensed Quasars in Large Imaging Surveys** towards the partial fulfilment of the BS-MS dual degree programme at the Indian Institute of Science Education and Research, Pune represents study/work carried out by Arjun Murlidhar at Indian Institute of Science Education and Research, Pune under the supervision of Dr. Anupreeta More, Research Faculty, Inter-University Centre for Astronomy and Astrophysics and Prof. Somak Raychaudhury, Vice-Chancellor, Ashoka University, during the academic year 2022-2023.

Dr. Anupreeta More

Prof. Somak Raychaudhury

Committee:

Dr. Anupreeta More

Prof. Somak Raychaudhury

Dr. Susmita Adhikari

We have peered into a new world and have seen that it is more mysterious and more complex than we had imagined. Still more mysteries of the universe remain hidden. Their discovery awaits the adventurous scientists of the future.

- Vera Rubin

Declaration

I hereby declare that the matter embodied in the report entitled **Searching for Quadruply Lensed Quasars in Large Imaging Surveys**, are the results of the work carried out by me at the Inter-University Centre for Astronomy and Astrophysics, Indian Institute of Science Education and Research, Pune, under the supervision of Dr. Anupreeta More and Prof. Somak Raychaudhury and the same has not been submitted elsewhere for any other degree.

Arjun Murlidhar

Acknowledgments

x

Abstract

Quadruply lensed quasars, where a lens galaxy produces four images of a background quasar, are powerful tools that can be used to study the expansion of the universe, galaxy evolution, and the nature of dark matter. These are a relatively rare occurrence, with fewer than a hundred quadruply-imaged systems of quasars known today. The next generation of ground and space-based telescopes like the Vera C. Rubin observatory and Euclid space telescope are expected to detect thousands of such strongly lensed quasars, which will allow us to do more precise science with these systems. In the first part of this thesis project, we explored the use of quadruply lensed quasars to identify groups of galaxies at intermediate redshifts. Quadruply lensed quasar images which are highly asymmetric point to the presence of a group/cluster of galaxies in the vicinity of the lens which contributes to the lensing. We studied the occurrence of such systems amongst the known quadruply lensed quasars and whether a group or cluster has been identified. In the second half of the project, we developed a prototype of a program to identify quadruply lensed quasar candidates in data from large surveys. The program utilizes the algorithm discovered by Schechter and Wynne (2019) to model quadruply lensed quasars. Initial tests of the program on mock lensed quasars and non-lenses showed promising results. We obtained a true positive detection rate of lensed quasars of over 90% and a false positive rate of $\sim 7\%$.

Contents

List of Figures

Chapter 1

Introduction

Gravitational lensing is a phenomenon in which light from a distant bright source (e.g. a quasar) is bent by the gravitational field of nearby objects (stars or galaxies). When this bending of light from a background source can lead to multiple images of the same source being seen, the phenomenon is called strong gravitational lensing [21, 14, 22]. Strongly lensed quasars are amongst the simplest gravitational lens systems consisting of a point-like source lensed by a galaxy-scale lens.

Quadruple-image systems of quasars are powerful tools to study galaxy evolution and cosmology. If variability is measurable in the lensed quasars, then the time delay in arrival of light from the different images can be used to measure the expansion rate of the universe [4, 6, 37]. Image positions and fluxes of the multiple images can be used to model the mass distribution of galaxies [40]. In fact, strong lensing provides much more information about galaxy mass distribution than dynamical observables for galaxies beyond the local universe [38]. Since lensing is sensitive to all mass, these images can be used to map the distribution of dark matter in a galactic halo and find its density profile [36]. Strong gravitational lenses have been used to detect substructures in dark matter halos of galaxies and place constraints on the nature of dark matter [19, 13].

One interesting application of quadruply lensed quasars is to use quads with highly elliptical configurations to find groups or clusters of galaxies in the vicinity of the lens that is causing this sheared configuration. Usually, images of the four quasars are distributed on a circle known as the Einstein Ring. There are exceptions, as in the lensed QSO B1422+231

[25] which is interesting because the configuration of the four images is not symmetrical, indicating a large external perturbation to the lensing [11] by a group or cluster of galaxies. This group was then directly observed using X-ray observations, and it was found that the lens galaxy belongs to this group. Since then, there have been several observations of quadruply lensed quasars with large external shear. If there is a large enough sample of lenses with high external shear, they can be used to derive a catalogue of groups at intermediate redshifts (where these lenses are usually found) which can aid in galaxy evolution studies.

The aim of the first part of this project was to survey the literature on lenses with large external shear, to find how many lenses with large external shear have been found, and to see if galaxy groups responsible for the shear have been identified.

While quadruply lensed quasars are very useful, they are also a rare phenomenon. There have only been around 60 quadruply lensed quasars discovered till date (a compilation of all lensed quasars discovered can be found here). Future surveys like the LSST, Euclid, and WFIRST are expected to detect hundreds of lensed quasars. But we need an efficient way to scour through terabytes of telescope data and identify potential lens candidates. For the remaining part of the project, we worked on building a program that can conduct an automated search for quadruply lensed quasars in large data sets.

There have been many searches for strong lenses, through imaging and spectroscopic surveys, but most of them were aimed at detecting lensed galaxies rather than just quasars [5]. Among the early large survey lensed quasar searches, the Cosmic Lens All-Sky Survey [20] found the largest sample of lensed radio quasars by identifying images with multiple quasars. The SDSS Quasar Lens Search used morphological and colour based selection on spectroscopically confirmed SDSS quasars [24]. In more recent years, there have been searches for lensed quasars using various methods which include magnitude and/or colour cuts [26], machine learning techniques [1], using the superior Gaia resolution to resolve blended sources and looking for multiple detections in candidates selected from other surveys [17], and using the time variability information of quasars [8].

In this thesis project, we focussed on a novel method to detect quadruply lensed quasars based on modelling the quasar image configurations (first demonstrated in [18]). The idea is that if a set of point sources are multiple images of the same quasar, then they must fit a lens model better than most random sources. The gravitational lens search robot CHITAH

[7] is an attempt to search for lensed double and quadruple quasars using a similar methodology. Our program uses a new algorithm to model quadruply lensed quasars discovered by Schechter and Wynne (2019) [29]. This is a simple method that exploits the geometry of lensed image configurations to fit a Singular Isothermal Ellipsoid model. The goodness of fit can be used to discriminate between lenses and random points of light. The advantage of this modelling technique is that it is much simpler and faster than conventional modelling of lenses, allowing us to run it on large data sets. Our program is specialised in searching only for quadruply lensed quasars. We have focussed on ensuring the program is fast and efficient so that we can run it on entire catalogs produced by surveys. We have tested the performance of the program on mock lensed quasar images based on the *Hyper Suprime-Cam* (HSC) survey. In the near future, we plan to run the program on actual data from the HSC survey.

This thesis is divided into four major chapters. In chapter 2 we discuss in brief the theory of gravitational lensing. we introduce the formalism of Fermat potential and discuss characteristics of multiply imaged quasar systems qualitatively, using the ideas of critical curves and caustics. In chapter 3, we discuss the work done in the first half of the thesis project on studying systems with large external shear. Chapters 4 and 5 are devoted to the second half of the thesis project. In chapter 4, we describe the algorithms being used in the program and the sample of mocks that were used to test the program. The results of these tests with mock lenses and non-lenses are discussed in chapter 5. Finally, we give a glimpse of the future directions of work.

Chapter 2

A Background on Gravitational Lensing Theory

The theory of gravitational lensing is based on the premise that light travels along null geodesics of a spacetime, as predicted by General Relativity. Thus, a theoretical model for gravitational lensing requires us to solve the geodesic equations to find the trajectory of a ray of light. This task is simplified by the assumptions made in GL theory.

The first assumption is that the gravitational field involved in lensing is weak. This is true if the Newtonian potential of the lens $\Phi \ll c^2$, and the velocity of the lens $v \ll c$. For a spherically symmetric mass distribution, this implies that the impact parameter of the light ray ξ, is much greater than the Schwarzschild radius R, $\xi \gg 2GM/c^2$. This is true for most astrophysical situations except, say, lensing by black holes or neutron stars.

Since the peculiar velocities of lensing galaxies are usually small compared to the speed of light, we will assume a stationary metric. The linearised metric for an isolated, stationary, perfect fluid source is given by

$$ds^2 = (1 + \frac{2U}{c^2})c^2 dt^2 - (1 - \frac{2U}{c^2})d\mathbf{x}^2 \tag{2.1}$$

where $U(\mathbf{x})$ is the Newtonian potential of the mass distribution. For a point source at the origin, $U(\mathbf{x}) = \frac{GM}{|\mathbf{x}|}$.

The second assumption, which is also very justified in most physical scenarios, is that the distances between the lens and source and lens and observer is much larger than any dimension of the lens. This means that the ray of light travels mostly undeflected between the source and lens and from lens to observer and is only deflected in a small region very close to the lens.

The above two assumptions also imply that the angles subtended by the source and lens as well as the deflection angle (defined as the angle between the initial and final ray directions) are all small.[21][31]

2.1   Fermat Potential and Time Delay

The path of a light ray under the assumptions of gravitational lensing can be found with the help of the following theorem,

Theorem 2.1.1. *(Fermat's principle) Let S be an event ("source") and l a time-like world line ("observer") in a spacetime. Then a smooth null curve γ, from S to l is a light ray (null geodesic) if, and only if, its arrival time τ on l is stationary under first-order variations of γ, within the set of smooth null curves from S to l [33],*

$$\delta\tau = 0$$

The proof of this theorem can be found in Schneider et al.1992 ([33]).

2.1.1   Geometry of lensing and lens equation

Consider the geometry of the source, lens, and observer as shown in Fig(2.1). By the second assumption of lensing, we can project the lens and source mass distributions onto planes at the mean source and lens distances, D_s and D_d. The positions of the source, lens, and observer are given by pairs of angles $\boldsymbol{\beta}$, $\boldsymbol{\theta}$, and $\hat{\boldsymbol{\alpha}}$. Since all angles are small, the distance in the lens plane can be approximated as $\boldsymbol{\xi} = D_d\boldsymbol{\theta}$, and that in the source plane, $\boldsymbol{\eta} = D_s\boldsymbol{\beta}$.
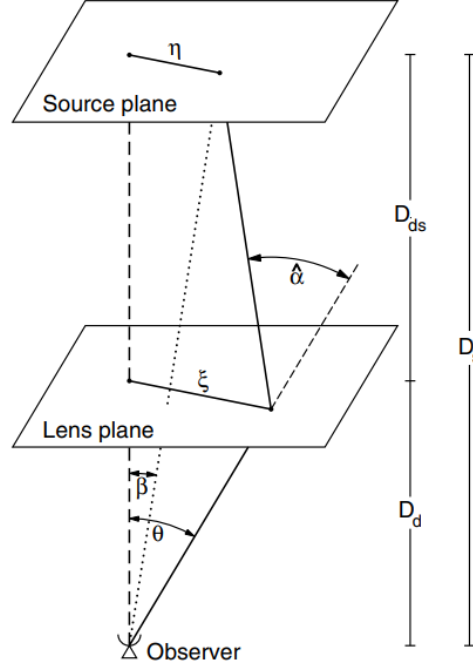
Figure 2.1: The geometry of lensing (Source: [31])

For a ray of light originating from a given point on the source plane, we can find a relationship between the point of intersection in the lens plane ("image position") and the deflection angle using the simple geometry defined above.

$$D_s\boldsymbol{\beta} = D_s\boldsymbol{\theta} - D_{ds}\hat{\boldsymbol{\alpha}}\left(\boldsymbol{\xi}\right) \implies \boldsymbol{\beta} = \boldsymbol{\theta} - \boldsymbol{\alpha}(D_d\boldsymbol{\theta}) \tag{2.2}$$

where, $\boldsymbol{\alpha} = \frac{D_{ds}}{D_s}\hat{\boldsymbol{\alpha}}$, is the scaled deflection angle. This angle depends on the mass distribution of the lens for a given source position and lensing geometry.

2.1.2 Fermat potential

In the thin lens and small deflection approximations, we assume that the actual ray path can be approximated as a combination of the incoming ray from S that will intersect the lens plane at I (Fig 2.1) and the outgoing ray from I to the observer O.

Let the ray originate from the source at $t = 0$, then the arrival time of the ray at the

observer O according to the metric in (2.1) is

$$t = \frac{1}{c} \int \left(1 - \frac{2U}{c^2}\right) dl = \frac{l}{c} - \frac{2}{c^3} \int U dl \qquad (2.3)$$

where l is the Euclidean path length and the second term is the contribution to the travel time due to the gravitational potential of the lens (Shapiro delay).

We can find the difference between the Euclidean path length of the ray in the presence of the lens and the path length between S and O without the lens. This is called the *geometric time delay* and is given by:

$$c\Delta t_{geom} = \frac{D_d D_s}{2 D_{ds}} (\boldsymbol{\theta} - \boldsymbol{\beta})^2$$

Similarly, we can evaluate the *gravitational time delay*. Define a two dimensional *deflection potential* $\psi(\boldsymbol{\theta})$ as

$$\psi(\boldsymbol{\theta}) = \frac{2 D_{ds}}{c^2 D_d D_s} \int U(\boldsymbol{\theta}) dl = \frac{4 G D_{ds} D_d}{c^2 D_s} \int d^2\theta' \Sigma(\boldsymbol{\theta}') \ln(|\boldsymbol{\theta} - \boldsymbol{\theta}'|) + const \qquad (2.4)$$

Adding the two contributions, the total time delay of a ray relative to an undeflected ray is given by

$$c\Delta t = \phi(\boldsymbol{\beta}, \boldsymbol{\theta}) + const \quad \text{where} \quad \phi(\boldsymbol{\beta}, \boldsymbol{\theta}) = \frac{D_d D_s}{D_{ds}} (\frac{1}{2}(\boldsymbol{\theta} - \boldsymbol{\beta})^2 - \psi(\boldsymbol{\theta})) \qquad (2.5)$$

$\phi(\boldsymbol{\theta}, \boldsymbol{\beta})$ is called the **Fermat potential**.

Theorem 2.1.1 says that the path of the light ray is given by the stationary points of the Fermat potential. Setting $\boldsymbol{\nabla}_\theta \phi = 0$, we get back the lens equation Eq(2.2):

$$\boldsymbol{\beta} = \boldsymbol{\theta} - \boldsymbol{\alpha}(\boldsymbol{\theta})$$

The deflection angle is given by, $\boldsymbol{\alpha} = \boldsymbol{\nabla}_\theta \psi$. The scaled deflection angle can be written in terms of $\boldsymbol{\theta}$ and a dimensionless surface mass density $\kappa(\boldsymbol{\theta})$ as:

$$\boldsymbol{\alpha}(\boldsymbol{\theta}) = \frac{1}{\pi} \int \, \mathrm{d}^2\theta' \kappa\left(\boldsymbol{\theta}'\right) \frac{\boldsymbol{\theta} - \boldsymbol{\theta}'}{|\boldsymbol{\theta} - \boldsymbol{\theta}'|^2} \tag{2.6}$$

where $\kappa(\boldsymbol{\theta})$ is called the *convergence* and is given by :

$$\kappa(\boldsymbol{\theta}) = \frac{\Sigma\left(D_\mathrm{d}\boldsymbol{\theta}\right)}{\Sigma_\mathrm{cr}} \quad \text{where} \quad \Sigma_\mathrm{cr} = \frac{c^2}{4\pi G}\frac{D_\mathrm{s}}{D_\mathrm{d}D_\mathrm{ds}} \tag{2.7}$$

Notice from Eq (2.6) and (2.7) that and $\nabla_\theta^2\psi(\boldsymbol{\theta}) = 2\kappa(\boldsymbol{\theta})$.

The constant in Eq (2.5) is the same for all rays from the source plane to the observer. Hence if we have multiple images, and we know image positions and redshifts of the source and lens, we can calculate the difference in arrival times of light from any two images,

$$c(t_1 - t_2) = \phi(\boldsymbol{\beta}, \boldsymbol{\theta_1}) - \phi(\boldsymbol{\beta}, \boldsymbol{\theta_2})$$

2.1.3 Cosmological corrections to the lens mapping equations

Till now we have investigated lensing in asymptotically flat and static spacetimes. This need not be true in our universe on the large scale. But the equations derived till now are mostly correct even in the realistic cosmological models we assume, albeit with a few small corrections.

Firstly all Euclidean distances D_d, D_s, and D_{ds} get promoted to *angular diameter distances*. The fermat potential (2.5) picks up a factor of $(1 + z_d)$ where z_d is the redshift of the lens [32].

$$\phi(\boldsymbol{\beta}, \boldsymbol{\theta}) = \frac{D_d^{ang} D_s^{ang}}{D_{ds}^{ang}}(1 + z_d)(\frac{1}{2}(\boldsymbol{\theta} - \boldsymbol{\beta})^2 - \psi(\boldsymbol{\theta})) \tag{2.8}$$

The lens equation 2.2 remains the same except all distances are now angular diameter distances. Angular diameter distances depend inversely on the Hubble constant H_o. If we have a variable source, we can measure the time delay between two images using the variation. Then, given all redshifts and image positions, for a given model of the mass distribution $\Sigma(\boldsymbol{\theta})$ and an estimate for other cosmological parameters, we can calculate H_o from 2.1.2. In the past couple of decades, this technique has been used to provide independent precise measurements of the Hubble's constant, in an attempt to resolve the Hubble tension.

2.2   Magnification

Gravitational lensing preserves surface brightness of the source. Recall, surface brightness is defined as the flux density per unit angular area of an extended object.

$$I^{(\text{image})}(\boldsymbol{\theta}) = I^{(\text{source})}[\boldsymbol{\beta}(\boldsymbol{\theta})] \tag{2.9}$$

The proof of the above statement can be found in Schneider's book ([34]). For a small solid angle $d\Omega$, $Flux = Surface\ Brightness \times d\Omega$. Therefore the ratio of flux densities of the unlensed image to the lensed image is given by,

$$\mu = \frac{Flux_{image}}{Flux_{source}} = \frac{d\Omega_{image}}{d\Omega_{source}} = \frac{d^2\boldsymbol{\theta}}{d^2\boldsymbol{\beta}}$$

This is exactly true for infinitesimal sources. The relation between area elements at $\boldsymbol{\theta}$ and $\boldsymbol{\beta}$ is given by the determinant of the jacobian matrix of the transformation between the two. Therefore, we can write the magnification as

$$\mu = \frac{1}{|det(\boldsymbol{A})|} \quad \text{where} \quad A_{ij} = \frac{\partial \beta_i}{\partial \theta_j} \tag{2.10}$$

2.2.1   Magnification matrix and distortion of images

Form of the magnification matrix: Consider the curvature tensor of fermat's potential,

$$\phi_{ij} := \frac{\partial^2 \phi}{\partial\theta_i \partial\theta_j} = \delta_{ij} - \frac{\partial^2 \psi}{\partial\theta_i \partial\theta_j} \tag{2.11}$$

Since $\frac{\partial\psi}{\partial\theta_i} = \alpha_i$, the curvature tensor is equal to the jacobian matrix of the transformation between $\boldsymbol{\beta}$ and $\boldsymbol{\theta}$, i.e., from 2.10 and 2.2,

$$\phi_{ij} = A_{ij}$$

. We know that,

$$\kappa = \frac{1}{2}(\psi_{11} + \psi_{22}) \tag{2.12}$$

Define,

$$\gamma_1 = \frac{1}{2}(\psi_{11} - \psi_{22}) \quad \text{and} \quad \gamma_2 = \psi_{12} = \psi_{21} \tag{2.13}$$

Then the Jacobian matrix can be written as,

$$\boldsymbol{A} = (1 - \kappa) \begin{pmatrix} 1 & 0 \\ 0 & 1 \end{pmatrix} - \gamma \begin{pmatrix} \cos(\chi) & \sin(\chi) \\ \sin(\chi) & -\cos(\chi) \end{pmatrix} \tag{2.14}$$

where $\gamma = \sqrt{\gamma_1^2 + \gamma_2^2}$ is called the *shear* and, $\tan(\chi) = \gamma_2/\gamma_1$. From (2.10), $\mu = \frac{1}{(1-\kappa)^2 - \gamma^2}$. $\boldsymbol{A}$ has eigenvalues $\lambda_{\pm} = 1 - \kappa \pm \gamma$.

Shape of images: Suppose a source centered at $\boldsymbol{\beta_o}$ produces two images cenetered at $\boldsymbol{\theta_A}$ and $\boldsymbol{\theta_B}$. If the angular size of the images are much smaller than the extent of the lensing potential, then we can assume a linear relation between image and source shapes. For a point on the image $\delta\boldsymbol{\theta}$ away from $\boldsymbol{\theta_A}$,

$$\delta\boldsymbol{\theta_A} = (\frac{\partial\boldsymbol{\theta}}{\partial\boldsymbol{\beta}})_A \delta\boldsymbol{\beta} = \boldsymbol{M_A}\delta\boldsymbol{\beta} \tag{2.15}$$

Similarly, $\delta\boldsymbol{\theta_B} = \boldsymbol{M_B}\delta\boldsymbol{\beta}$. Here, $\boldsymbol{M(\theta)} = \boldsymbol{A(\theta)}^{-1}$, is the *Magnification matrix*. If in (2.14) the shear $\gamma = 0$, then $\boldsymbol{M_A}$ will be a diagonal matrix and each dimension of the image will get magnified by a factor of $1/(1-\kappa)$ relative to the source. Thus the convergence term magnifies or de-magnifies the source without changing its shape. Whereas if we have only

the shear term γ, then we get a general shear transformation.

We cannot measure directly the matrices M_A or M_B since we do not observe the source. What we can measure is the transformation matrix between the two images,

$$\delta\boldsymbol{\theta_B} = (\boldsymbol{M_B}\boldsymbol{M_A}^{-1})\delta\boldsymbol{\theta_A} = \boldsymbol{M_{BA}}\delta\boldsymbol{\theta_A} \tag{2.16}$$

The determinant of this matrix is the ratio of the fluxes of the two images.

2.3   Classification of Images and the Odd Number Theorem

First a few definitions.

Definitions 2.3.1. *Critical Curves: The set of lines in the image plane where $det(\boldsymbol{A}) = 0$ i.e., the magnification diverges.*
Caustics: The curves in the source plane that the critical curves map to according to the lens mapping equation (2.2).
Ordinary Images: Images for which $det(\boldsymbol{A}) \neq 0$ i.e., images that do not form on critical curves.

Ordinary images thus form where the Fermat potential attains an extremum, $\nabla\phi = 0$ and the Jacobi matrix ϕ_{ij} does not have any zero eigenvalues. Extrema of ϕ can be of three types,

Type I: Minimum of ϕ. The minimum is characterized by positive definiteness of $\boldsymbol{A}$. This means that both eigenvalues of $\boldsymbol{A}$ are positive. $det(\boldsymbol{A}) > 0$ and $Tr(\boldsymbol{A}) > 0$.

$$1 \geq (1 - \kappa) > \gamma > 0, \quad \mu \geq 1$$

Type II: Saddle point of ϕ. The saddle point is characterized by eigenvalues of opposite sign. $det(\boldsymbol{A}) < 0$

$$(1 - \kappa)^2 < \gamma^2$$

Type III: Maximum of ϕ. The maximum is characterized by negative definiteness of $\boldsymbol{A}$. This means that both eigenvalues of $\boldsymbol{A}$ are negative. $det(\boldsymbol{A}) > 0$ and $Tr(\boldsymbol{A}) < 0$.

$$(1 - \kappa)^2 > \gamma^2, \quad (1 - \kappa) < \gamma, \quad \kappa > 1$$

The sign of the determinant of $\boldsymbol{A}$ is called the parity of the image. Images of type I and III have positive parity and images of type II have negative parity. Positive parity images preserve the handedness of images whereas negative parity images reverse it. Let two vectors $\boldsymbol{X}$ and $\boldsymbol{Y}$ in the source plane map to two vectors $\boldsymbol{W}$ and $\boldsymbol{Z}$ in the image plane. Handedness is then defined as the sign of $\boldsymbol{X} \times \boldsymbol{Y}$ or $\boldsymbol{W} \times \boldsymbol{Z}$.

Odd Number Theorem: Consider a geometrically thin GL with a smooth surface mass density $\kappa(\boldsymbol{\theta})$ which decreases faster than $|\boldsymbol{\theta}|^{-1}$ as $|\boldsymbol{\theta}| \rightarrow \infty$. Let n_I, n_{II} and, n_{III} be the number of images of each of the three types and let n be the total number of images. Then,

Theorem 2.3.1. *Under the above assumptions, provided the source does not lie on a caustic,*
(a) $n_I \geq 0$ and $n = n_I = 1$ for large $\boldsymbol{\beta}$ (i.e., source position tending to infinity).
(b) $n < \infty$ and images are isolated, i.e., they cannot accumulate.
(c) $n_I + n_{III} = 1 + n_{II}$. Therefore, total number of images $n = 1 + 2n_{II}$ is odd and $n > 1$ iff $n_{II} \geq 1$.

The proof for the above theorem can be found in [35]. The odd number theorem says that all gravitational lens systems produce an odd number of images. They will have at least one image that corresponds to a minima of the potential and hence be magnified relative to the source.

The most common configurations produced by galaxy scale lenses are 1, 3, and 5 image geometries. When the source is far from the center of the lens, one image is produced. In other cases, we see 2 or 4 images. This is because one image is always produced on top of the lens galaxy and is usually demagnified.

2.4   Critical Curves and Caustics

Qualitative properties of lensed systems like the number and type of images and their rough positions can be deduced by observing the position of the source with respect to the caustic curves.

Consider a point source. If the source is far away from the lens center, the Fermat potential has only one minimum. For all real lenses, the deflection angle tends to zero as $|\boldsymbol{\theta}|$ tends to infinity. Therefore for large enough $|\boldsymbol{\beta}|$, $\boldsymbol{\theta} \approx \boldsymbol{\beta}$.

At a caustic, the determinant of the Jacobian, $det(\boldsymbol{A}) = 0$. Therefore, the magnification of the point source formally diverges (though in reality, we don't have perfect point sources, and the geometric optics approximation breaks down here). A source close to a caustic produces a highly magnified image close to the corresponding critical curve. When the source crosses this caustic (in the direction towards the lens center), two images are created on either side of the critical curve. If the source moves past this caustic in the opposite direction, these two images will merge and disappear.

The eigenvalues of $\boldsymbol{A}$ must vary continuously as the source moves around in the source plane. At a critical curve, one of the eigenvalues of $\boldsymbol{A}$ goes to zero. Hence, this eigenvalue has opposite signs on either side of the critical curve. Therefore, critical curves divide the lens plane into regions of positive and negative parity.

From Eq (2.15) we can see that if one of the eigenvalues of $\boldsymbol{A}$ goes to zero, then the image will be highly stretched in the direction of that eigenvector. Extended sources near caustics have images that are stretched into arcs.

2.5   A Simple Model: The Circularly Symmetric Lens

We will wrap up this lightning review of the theory of gravitational lensing by considering a simple model of an axially symmetric lens. While in reality, perfectly circular/spherical lenses do not exist, some of the general features we encounter in this case carry forward to more complicated models.

Lens Equation: For circularly symmetric lenses, the surface mass density is a function of only the magnitude of the image position vector, $\Sigma(\boldsymbol{\theta}) = \Sigma(|\boldsymbol{\theta}|)$. We will discuss a general circularly symmetric lens without alluding to a specific form of $\Sigma(\theta)$ for now. The deflection angle points inwards radially and is given by:

$$\alpha(\theta) = \frac{2}{\theta} \int_0^\theta \theta d\theta \kappa(\theta) \tag{2.17}$$

The lens equation can be written as,

$$\boldsymbol{\beta} = \boldsymbol{\theta}[1 - \alpha(\theta)/\theta] = \boldsymbol{\theta}[1 - \langle \kappa(\theta) \rangle], \tag{2.18}$$

where

$$\langle \kappa(\theta) \rangle = \frac{2}{\theta^2} \int_0^\theta \theta d\theta \kappa(\theta) = \alpha(\theta)/\theta \tag{2.19}$$

is the average convergence inside a radius of θ.

Critical curves and the Einstein Radius: We can use the lens equation to calculate the Jacobian matrix $\boldsymbol{A}$. It turns out that we can write the magnitude of the shear as $\gamma = (\langle \kappa(\theta) \rangle - \kappa(\theta))$. The angle of the shear χ is the same as the polar angle, i.e., $\boldsymbol{\theta} = \theta(\cos(\chi), \sin(\chi))$. The eigenvalues of A are $1 - \langle \kappa(\theta) \rangle$ and $1 + \langle \kappa(\theta) \rangle - 2\kappa(\theta)$. As we can see, circularly symmetric lenses have two circular critical curves at θ defined by setting each of the eigenvalues to zero. The critical curve obtained by setting the first eigenvalue to zero is called the tangential critical curve. This is because images formed on this critical curve are elongated in the tangential direction (along the boundary of the circle). The other critical curve is called the radial critical curve, since images are elongated in the radial direction.

The tangential critical curve is defined by the condition $\langle \kappa(\theta) \rangle = 1$ which means that the mean surface mass density inside this radius is always equal to the critical density. The radius of this critical curve is called the *Einstein radius.* From Eq (2.18) we can see that, every point on this critical curve is mapped to the point $\boldsymbol{\beta} = 0$ in the source plane, i.e., the tangential caustic degenerates to a point because of the high symmetry.

The radial caustic is usually a circle in the source plane. If a source is exactly aligned with the center of the lens, then its image is stretched out into a ring at the Einstein radius

(a) Source outside the radial caustic produces a single image outside both critical lines

(b) 2 Image geometry: Source crossing the first caustic produces two additional images on either side of the corresponding critical line. The central image is demagnified.

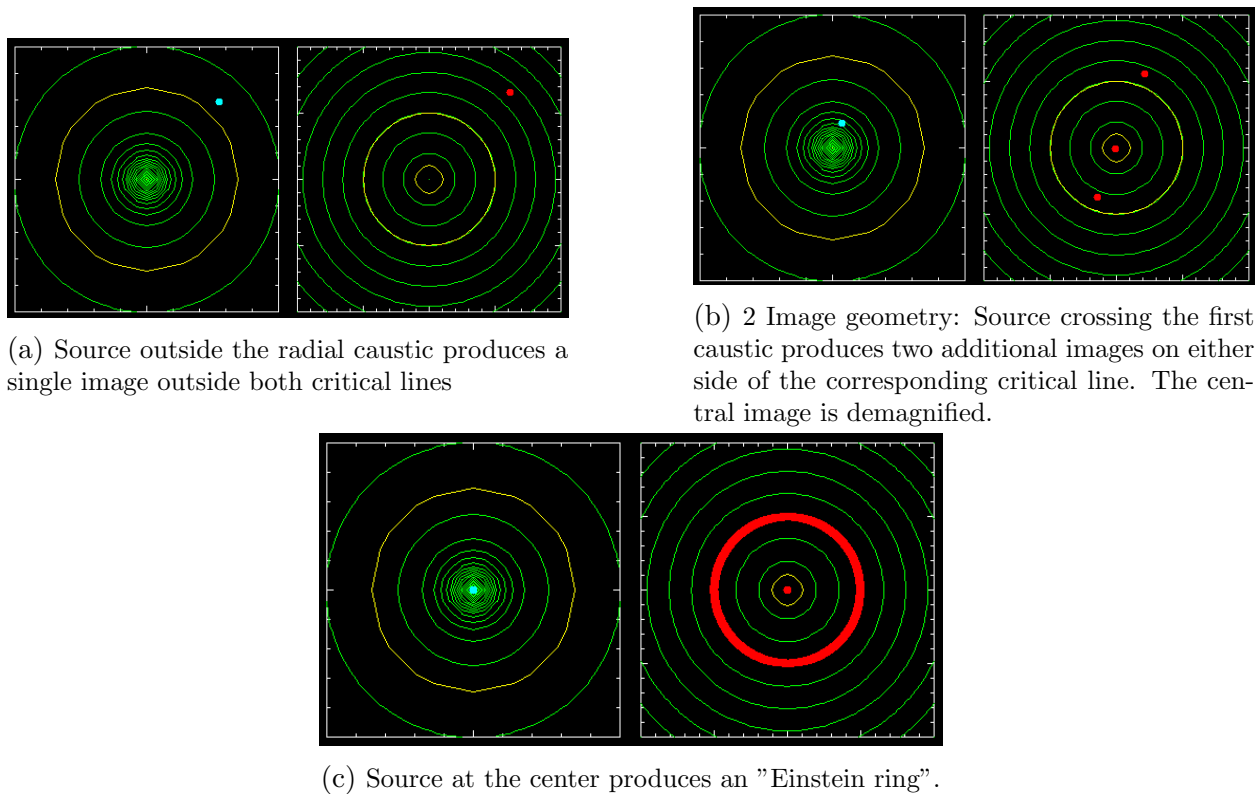(c) Source at the center produces an "Einstein ring".

Figure 2.2: **Circularly symmetric lens model:** A circularly symmetric lens model. The left panel of each image shows the lens mass profile (green), caustics (yellow), and source position (blue dot). The right panel shows the deflection potential (green), critical curves (yellow) and image positions (red dots). These images were generated from the SimpLens [28] app found on Prasenjit Saha's webpage.

along with an image at the center of the lens ($\theta = 0$). If we can identify arcs or images that trace the Einstein radius, we can use this to calculate the mass enclosed within this radius. The Einstein radius is also the best determined parameter of the lens since all models find almost the same value for it (ref?).

The tangential caustic point is sensitive to small perturbations that break the circular symmetry. In the presence of any ellipticity in the mass model of the lens or external perturbation, this caustic unfolds into a curve of finite extent (usually with an astroid-like shape). If the source crosses this curve, two additional images are produced at the tangential critical curve.
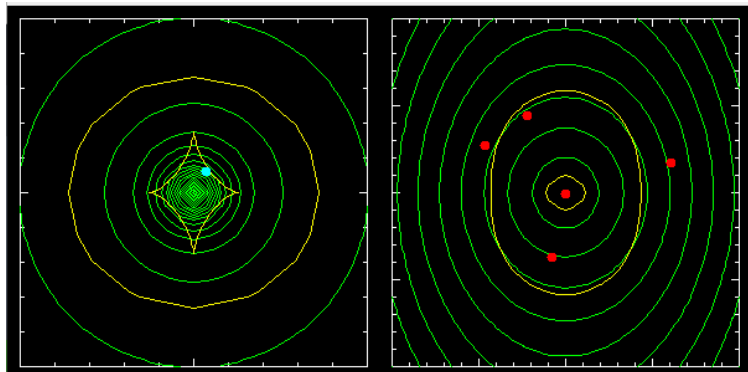
Figure 2.3: **Non-circular lens model:** Circularly symmetric lens with external perturbation. The tangential caustic is now an astroid. A source inside this caustic produces five images of which four are usually detectable.

Chapter 3

External Shear - Galaxy Group Connection

3.1 External Shear

External shear refers to the perturbation to the potential of the lens by an external source of mass. Most galaxies are today believed to exist in complex environments consisting of other galaxies in groups or clusters. The potential of this group or cluster is expected to contribute to the lensing by the lens galaxy. Even if we assume a perfectly spherically symmetrical galaxy, this symmetry will be broken by the external perturbation.

Since the scale of groups and clusters of galaxies is much larger than the scale of lensing by an individual galaxy, we can safely assume that the potential due to this group changes slowly over the extent of the Einstein ring of the lens galaxy ($\sim 1^{"}$). In order to find the contribution of the group/cluster to the lensing, we can Taylor expand the deflection potential (Eq 2.4) about the center of the lens galaxy. Assuming the lens galaxy is at the center of the cluster/group, the first term with observable consequences is,

$$\Psi_p(\boldsymbol{\theta}) \simeq \frac{1}{2}\boldsymbol{\theta} \cdot \nabla\nabla\Psi_p \cdot \boldsymbol{\theta} = \frac{1}{2}\kappa_p|\boldsymbol{\theta}|^2 - \frac{1}{2}\gamma_{p,1}(\theta_1^2 - \theta_2^2) - \gamma_{p,2}\theta_1\theta_2 \qquad (3.1)$$

The external convergence term, κ_p, only makes a difference when measuring time delays.

This is because, in the lens equation derived from this potential, we can re-scale all angles by the convergence. This will only lead to a change in the source position and deflection potential. If we do not have an independent estimate of the lens mass, then neither of the quantities are observable. The rescaling of the deflection potential is equivalent to adding a sheet of constant surface density to the lens mass model. This is known as "mass sheet degeneracy" [10]. The external shear terms $\boldsymbol{\gamma}_p$ leads to a change in the image configuration.

In a perfectly circularly symmetric lens, the inner caustic collapses to a point aligned with the center of the lens. If a source is placed exactly behind the lens, it is stretched onto a ring around the lens (Fig 3.1a). A tiny perturbation causes this ring of images to break up into four images arranged on a circle (Fig 3.1b). This perturbation could either be a deviation from circular symmetry of the mass distribution or an external perturbation from another galaxy or a group of galaxies in the immediate environment of the lens.
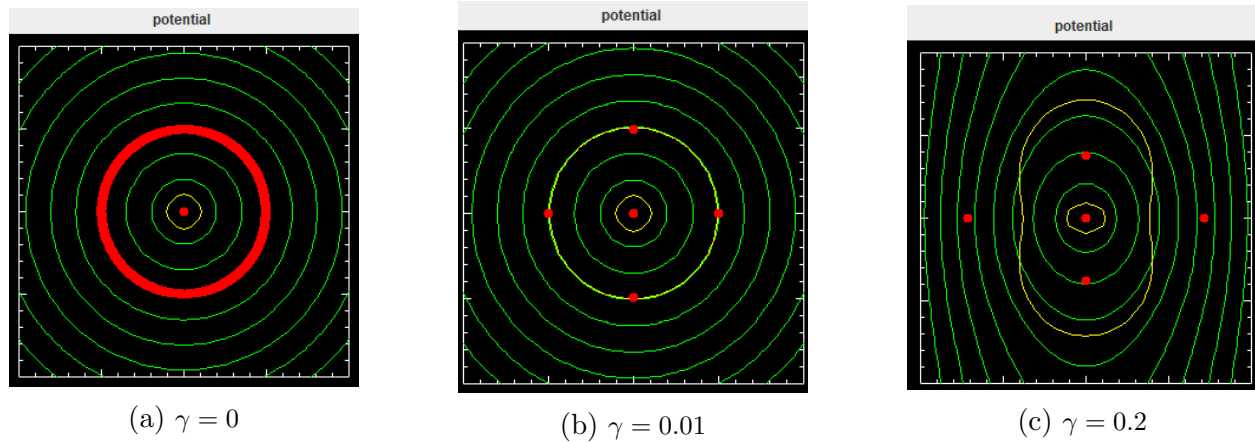

(a) $\gamma = 0$ (b) $\gamma = 0.01$ (c) $\gamma = 0.2$

Figure 3.1: **Effect of external shear:** A circularly symmetric lens with external shear γ and with the source placed at the center of the lens potential. The green contours show the lens mass density profile, the yellow contours are critical curves, and the red dots are image positions. These images were generated from the SimpLens [28] app found on Prasenjit Saha's webpage.

As the strength of this perturbation increases, the configuration of the four images becomes more and more elliptical (Fig 3.1c). Therefore, a large eccentricity of the ellipse that passes through the four images indicates a large perturbation. Although the perturbations due to the ellipticity of the mass distribution and external mass behave similarly, we do not expect lens galaxies to usually have very large ellipticities. Hence, such systems are usually indicative of a large external shear.

3.1.1 External Shear - Galaxy Group Connection

As explained above, external shear is the quantification of the perturbation due to an external galaxy or group of galaxies. Therefore, it is reasonable to assume that quadruply lensed systems that require a large external shear in the modelling of the lens potential could be part of a group of galaxies. An example to support this hypothesis can be found in the paper by Raychaudhury et al [25], where they study the lens B1422+231 - a system that is dominated by external shear. The authors were able to detect X-ray emission from the group that the lens belongs to and this group is able to account for all the external shear.

In line with this, during the initial part of the project, we sought to use quadruple lenses with large external shear to find galaxy groups associated with them. If we have a large enough sample of lenses with significant external shear, we can use that to derive a sample of galaxy groups at intermediate redshifts, which are often hard to detect directly.

As a first step towards this, we decided to do a survey of all the quadruple lenses discovered till now in order to find the fraction of lenses with large external shear.

3.2 Apparent Shear Ellipse

If we were to fit ellipses to the four image positions in quadruple lenses, we know that lenses with higher external shear should have ellipses with larger eccentricities.

Saha and Williams [27] describe a way to do this in something they call the *apparent shear ellipse*. They consider ellipses of the form,

$$\frac{1}{2}\left(\boldsymbol{\theta} - \boldsymbol{\beta}'\right)^2 + \frac{1}{2}\gamma_1'\left(\theta_x^2 - \theta_y^2\right) + \gamma_2'\theta_x\theta_y = c \tag{3.2}$$

This looks like the fermat potential (Eq 2.5) for a lens with external shear (Eq 3.1) without the contribution from the convergence term or deflection potential of the galaxy. Equation (3.2) has five unknown parameters: $\beta_x, \beta_y, \gamma_1', \gamma_2',$ and c. These can be determined by demanding the four images lie on the ellipse and that the total shear $\gamma' = \sqrt{\gamma_1'^2 + \gamma_2'^2}$ is minimized.

$\gamma^{'}$ is called the apparent shear and is indicative of the actual shear. Apparent shear is related to the eccentricity of the ellipse in a simple way,

$$e^2 = \frac{2\gamma^{'}}{1 + \gamma^{'}}$$

As seen above, eccentricity increases monotonically with apparent shear.

3.3 Results

We ran the code to fit apparent shear ellipses on a sample of 38 quadruple lens systems out of the ~ 60 quadruple lenses that have been discovered.

The histogram of the fit can be found below. The sample had an average apparent shear of 0.228 and a standard deviation of 0.175. We then selected 6 quads with large apparent shear and searched the literature to see if the environments of these quads have been investigated, the results of which have been summarized below.
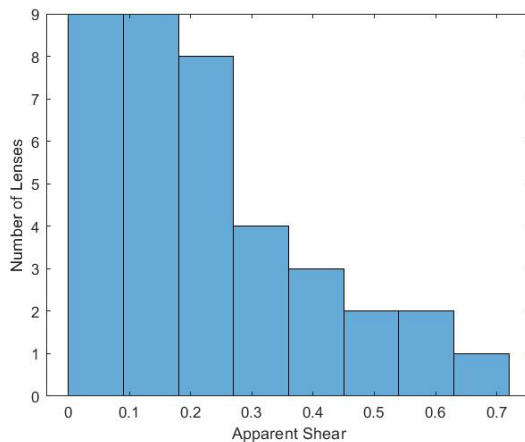

Figure 3.2: Histogram of apparent shear distribution

3.3.1 Notes on quads with large apparent shear

J2211-0350: Apparent Shear = 0.72. Modelled in Daniela Bettoni et al 2019 [3]. They find an SIE+XS fits the images well with q = 0.66 and external shear, gamma= 0.31. This

lens is found on the edge of the cluster RXC J2211.7-0350 to which they attribute the large external shear.

J0029-3814: Apparent Shear = 0.62. Modelled by STRIDES 2022 [30] and TD-COSMO XI [9]. Both find an external shear of ~ 0.2. TDCOSMO say it is "possibly due to the overdense environment to the North of the lensing system".

2M1134-2103: Apparent shear = 0.60. Modelled by Rusu et al, 2019 [26]. They fit an SIE+XS model and find external shear of 0.39 and axis ratio of 0.80. The shear is attributed to a nearby galaxy and a possible group of ~ 50 or more galaxies, though only a few galaxies of the proposed group are visible.

DES J0053-2012: Apparent shear = 0.48. Modelled by Lemon et al, 2020 [16]. They find that this system is not adequately modelled by a single SIE+XS but requires one to explicitly fit an SIE to a companion galaxy (redshift undetermined). This gives an external shear of 0.13.

J0818-2613: Apparent shear = 0.45. Modelled by Lemon et al, 2022 [15] and Stern et al 2021 [39]. Lemon et al find that it requires an SIE + XS with mass ellipticity = 0.6 and external shear = 0.38 perpendicular to mass ellipticity and a large Einstein radius ($\sim$ 3"). No group or cluster found. Stern et al suggest that a group or cluster may lie along the line of sight.

PSJ0147+4630: Apparent shear = 0.32. Modelled by Berghea et al, 2017 [2]. SIE + XS model requires external shear of 0.14 and an ellipticity of 0.17. No mention of groups or clusters.

As we can see, in most cases, a search for groups has already been done for the small number of lenses with large external shear. We realised that further work in this direction was limited by the number of quadruply lensed quasars that have been discovered. This motivated us to shift our focus toward searching for quadruply lensed quasars which we worked on during the second half of this project.

Chapter 4

Lens Search: The Algorithm

In the second half of this master's thesis, we worked on building a program for the automated detection of quadruply lensed quasars in data from imaging surveys. The code we built will work on image cutouts from telescope surveys and will classify images with four point-like sources as being potential lens candidates or random sources of light. We have focused on developing this software to search for quads in data from the HSC survey. The code is divided into three parts. The first part will use quasar and lens color information to subtract lens light from the image. The second part will use this lens-subtracted image to identify the positions of the four point sources. Finally, the third part will use these positions to fit the Schechter-Wynne [29] model and determine if the point sources are lensed quasars or four-point sources aligned by chance.

At the time of writing this thesis, we built and tested the last two steps of the program - finding the positions of the quasars and fitting the Schechter-Wynne model. In the rest of this chapter, we will describe in detail the two parts of the code we have written.

4.1   Position Finder

The Position Finder code finds accurate astrometry of the quasar images by identifying local peaks in pixel brightness. If all four positions have not been found in the first run, the algorithm improves its performance by subtracting the positions found in the first run from

the image and attempting to find the remaining positions from the subtracted image.

4.1.1   The algorithm

1. *Find all the local peaks in the lens-subtracted image.*

   We are using the `find_peaks()` function from the photutils module for local peak detection. `find_peaks()` finds peaks in an image as the maxima above a given threshold in a specified local region. The local region is defined by a square box of a particular *box size* around each pixel. Two maxima are separated by at least *box size* pixels. Since quasars can be considered as point sources whose flux is smeared by a psf, we can expect quasar images to have clear peaks at the position of the image. The box size is set as 5 pixels for this first run. Threshold is defined as mean background level $+ 5 \times$ (standard deviation of bg). This is the minimum value a pixel must have to be considered as a local peak. The threshold is chosen keeping in mind the threshold for considering a pixel to be part of a source in the HSC survey. Background mean and standard deviation are calculated using `sigma_clipped_stats()` function from photutils. This estimates background statistics by sigma-clipping any sources. The image cutout without the central region (where the lens lies) is used to estimate the background. Once a peak is found, `find_peaks()` finds the centroid within the local region centered on the peak pixel. It does this by fitting a 2D gaussian to the pixels. This gives us the position of the image up to sub-pixel precision.

2. *Identify contaminants that do not belong to the lens system.*

   The image cutout, which is centered on the lens, might have other background/ foreground galaxies and stars. Since the angular scale of the lens system is ~ 1", any peak found outside this radius from the center is not expected to belong to the lens system. In this step, we identify all peaks outside a radius of 2" as being contaminants.

3. *If less than 4 quasar images have been found, create a model image that replicates the fluxes and positions of the quasars and contaminants*

   This is done by creating a model image with positions found in the previous step, starting with random magnitudes for the images. This model image is convolved

with the appropriate psf produced by the HSC survey. In order to obtain the correct magnitudes of the different images, the code minimizes the sum of the squared difference between the two image arrays, normalized by the variance of the background. We use a global optimization algorithm `differential_evolution()` from the *Scipy* library for this.

4. *Subtract the model image from the actual image and find the remaining peaks*

On subtracting the two images, the code uses `find_peaks()` to find the remaining quasars. This time, we use a box size of 3. Suppose we found x quasars in the first run and need to find $n = 4 - x$ more quasars. If more than n peaks are found by the peak finder in this run, then it selects only the brightest n peaks to return. This is done because the magnitude modeling will have some errors. These errors lead to an imperfect subtraction with residual light left behind by the subtracted quasars. This residual light will be dimmer than the remaining quasars to be found in most cases. Hence choosing the brightest n peaks will ensure that we do not pick up such residuals.

5. *If extra quasar(s) were found in the previous step and all 4 quasars have not been found yet, repeat steps 3,4,5.*

The flux modeling, subtraction, and peak finding steps are repeated until (a) Four quasar positions are recovered, or (b) The number of peaks found does not increase from the previous run of the three steps.

(a) Mock lensed quasar image   (b) Model image replicating two quasar positions and fluxes   (c) Model image subtracted from actual image.
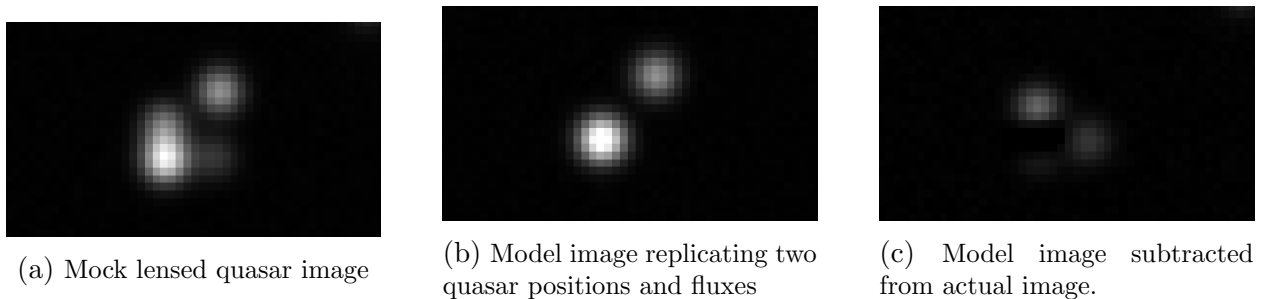
Figure 4.1: **Position Finder Demonstration:** An sample mock lensed quasar image run through the Position Finder. Fig (a) is the actual mock lensed quasar image. In the first run Position Finder identified two of the four quasar images. It then created a model image replicating the flux and positions of the two quasars (Fig (b)). On subtracting the actual image from the model image, we are left with the two unidentified quasars in Fig (c). Position Finder ran the peak finding algorithm again on this image and successfully found the remaining two positions.

4.2   Schechter-Wynne Algorithm

Schechter and Wynne in 2019 [29] found a simple way to model quadruply lensed quasars using an SIEP model. Drawing from the work of Witt [41], they showed that the lensed quasar positions due to a lens with a Singular Isothermal Ellipsoid (SIE) potential lie at the points of intersection of an "amplitude" ellipse and a rectangular hyperbola ("Witt hyperbola"). Therefore, given four points of light, we can try to fit the prescribed ellipse and hyperbola passing through the points. The goodness of fit can be used as a figure of merit to distinguish between lenses and random points of light.

4.2.1   The amplitude ellipse and Witt hyperbola

SIE is a mass model for galaxies with elliptical isodensity contours. It is widely used to model lens galaxies and is quite successful in approximating actual lens potentials [12]. Let us refer to the frame in which the axis of the deflection potential is aligned with the x and y axes as the "aligned frame". The deflection potential for the SIEP in this frame is given by:

$$\psi(x,y) = a^2 \sqrt{\frac{(x-x_g)^2}{a^2} + \frac{(y-y_g)^2}{q^2 a^2}} \tag{4.1}$$

where (x_g, y_g) is the position of the lens galaxy, a is the x semiaxis, and q is the axis ratio. Given this potential, there exists an ellipse centred on the source position, with axes aligned with the potential, and which passes through all four image positions [42] called the *amplitude ellipse*,

$$\frac{(x-x_s)^2}{a^2} + \frac{(y-y_s)^2}{a^2/q^2} = 1 \tag{4.2}$$

The axis ratio of the amplitude ellipse, $1/q$, is the inverse of that of the potential. The images also lie on a rectangular hyperbola whose asymptotes are aligned with the potential and amplitude ellipse [41].

$$(x - x_g)(y - y_s) = \frac{1}{q^2}(y - y_g)(x - x_s) \tag{4.3}$$

The hyperbola passes through both the source and lens positions.

4.2.2 The algorithm

Schechter and Wynne [29] in their 2019 paper have detailed a recipe for modeling the quasar positions using the amplitude ellipse and Witt hyperbola. The algorithm is as follows:

1. *Find the rectangular hyperbola passing through the four image positions in the observed frame.*

   We can write the general equation of a rectangular hyperbola as $A(x^2 - y^2) + xy + Cx + Dy + E = 0$. The four quasar positions will give us four linear equations with which we can determine the unknown coefficients A, C, D, and E.

2. *Find the image coordinates in an "aligned" frame with axes parallel to the asymptotes of the hyperbola.*

   In general, the observed frame need not be the same as the aligned frame. The hyperbola that we fit in the first step will give us the angle which the aligned frame makes with the observed frame,

   $$\theta = -\frac{1}{2}\arctan(2A) \tag{4.4}$$

   We can then find the image coordinates in this frame.

3. *Find the amplitude ellipse passing through the four image positions and aligned with these axes.*

   The equation of the amplitude ellipse in the aligned frame is given by Eq 4.2. We can use this equation to fit the image coordinates found in step 2 (which are in the aligned frame). The equation of the amplitude ellipse in the aligned frame is given by $x^2 + C_e y^2 + D_e x + E_e y + F_e = 0$, where $C_e = q^2$, $D_e = -2x_s$, $E_e = -2y_s q^2$, and $F_e = x_s^2 + q^2 y_s^2 - a^2$. From the above relations, we can find the source position (x_s, y_s), axis ratio q, and the semi-axis a.

4. *Find the two images subtending the smallest angle from the center of the amplitude ellipse.*

5. *Evaluate Witt's equation 4.3 at the positions of these two images to solve for the unknown coordinates of the lensing galaxy, (x_g, y_g).*

> The equation of the Witt hyperbola in the aligned frame can be written as $B_h xy + D_h x + E_h y + F_h = 0$, where $B_h = q^2 - 1$, $D_h = y_g - y_s q^2$, $E_h = x_s - x_g q^2$, and $F_h = x_g y_s q^2 - y_g x_s$. We know $q, x_s,$ and, y_s from step 3. Therefore we need only two of the quasar positions to find the remaining unknown coefficients (x_g and y_g) in the equation above. If our lens is exactly modeled by an SIE potential, then the hyperbola will pass through the remaining two quasar positions as well. But in reality, there will be an offset between the predicted positions (at the intersection of the hyperbola and ellipse) and the actual positions for the remaining two quasars. The amount of offset can be used as a figure of merit to determine whether the four images are due to a lensed quasar or if they are random points of light. We choose to fit the hyperbola to the pair of closest quasars since this guarantees a four-image model [29]. This model will also reproduce the separation of the closest pair which can be used to predict their fluxes.

In the above process, there are several exceptional cases that could occur. If $C_e = q^2 < 0$, then the curve fit in the third step will be a hyperbola and not an ellipse. For such systems we cannot fit an SIEP model and hence are not likely to be lensed quasars. Similarly, if in step 3 we are not able to fit an ellipse because the matrix of the linear equations is singular, or if the axis ratio q is too large or zero, then the system is unlikely to be a quadruply lensed quasar. The program automatically classifies all such cases where the algorithm has failed in some step as a non-lens.

In order to find the predicted positions of the two quasars not fit by the hyperbola, we need to find the two remaining points of intersection of the ellipse and hyperbola. We are using a python package (github) for numerically finding the points of intersection of the ellipse and hyperbola. We are then cross-matching the observed and predicted sets of points to identify which of the intersections correspond to the quasars not fit by the hyperbola. The root-mean-square offset of these quasar positions from their predicted positions is calculated and is normalized with the semi-axis a. This normalized rms offset is used as the figure of merit.
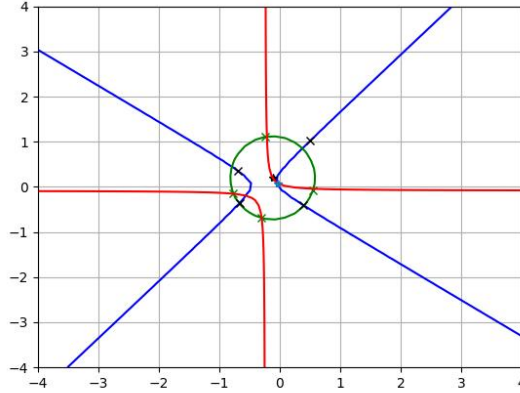
Figure 4.2: **Schechter-Wynne Algorithm Demonstration:** A sample mock lensed quasar image run through the SW algorithm. The four black crosses are the original quasar image positions. The blue rectangular hyperbola is the first hyperbola fit to all four points. The green crosses represent quasar image positions in the frame aligned with the asymptotes of the blue hyperbola. The green ellipse (SW ellipse) fits all four quasar positions in the aligned frame. The red hyperbola (Witt hyperbola) passes through two closest image positions. The remaining two quasars are slightly offset from the Witt hyperbola.

4.3 Mock Lenses and Non-Lenses

In order to test the algorithms described above, we created a set of 617 mock quadruply lensed quasars and 500 mock non-lenses.

4.3.1 Mock Lensed Quasars

Mock lenses were created using the strong lensing analysis software *glafic* [23]. Glafic takes as input a lens mass model, light profile, redshift and point source redshift, position, and flux to find the lensed image of the point source. Quasar redshifts and fluxes in different bands were taken from an HSC quasar catalog. Similarly, lens redshifts and cmodel magnitudes were picked randomly from the list of extended objects in the HSC pdr3 wide forced catalog. Quasars that are around a redshift of 2 and lens galaxies around a redshift of 0.5 were chosen. This combination of source-lens redshifts is most commonly found in lensed quasars. For the mass model of the lens, we chose an SIEP model. Velocity dispersions of the lens galaxy were chosen to be in a small interval around 220 km/s. This corresponds to an Einstein radius ~ 1 arcsec. Ellipticity and position angle of the galaxies were chosen randomly in

a typical range. For the light profile of lenses, we used a de Vaucouleurs model. We used the luminosity-effective radius relation from Eq 15 of [24]. Positions of the sources were randomly chosen while ensuring that they lie within the tangential caustic so that we get four images. These lensed sources were then added to cutouts of empty regions from HSC images to simulate realistic backgrounds.

4.3.2   Mock Non-Lenses

Mock non-lenses were created by randomly placing four point sources within a 4.5×4.5 arcsec square. The positions were chosen such that in each image at least one pair of quasars had a separation of less than 1 arcsec. This would allow us to test the performance of the position finder. The point sources were chosen to have a magnitude between 21 and 25 and were convolved with the HSC g-band PSF. Background sky and noise were chosen based on typical values found in HSC g-band cutouts.

Chapter 5

Lens Search: Results

Both the mock lenses and non-lenses were used for testing the position finder and Schechter-Wynne algorithms. The results of those tests are described in this chapter.

5.1 Position Finder Tests

5.1.1 Non-Lenses

Of the 500 non-lenses that were run on the position finder, the algorithm could identify all four positions correctly in 378 of them, which gives it a success rate of $\sim 75.6\%$. A successful identification corresponds to identifying the quasar positions within 1.5 pixels of their true position (where the dimension of a pixel is 0.168"). We can understand this better if we look at its rate of success with respect to the quasar magnitudes and separations in the images.

From Fig (5.1a) we can see that the algorithm is able to detect quasar pairs well up to a separation of 0.5". Below this, the rate of detection falls below 50%. The algorithm is also able to detect quasars of all magnitudes fairly well. Its performance reduces to around 80% for magnitudes close to 25.

The cases where the algorithm has failed clearly seem to be where the separation between two quasars is small. In order to see whether the relative magnitudes of the pair of quasars

(a) Distribution of minimum separation

(b) Distribution of magnitudes
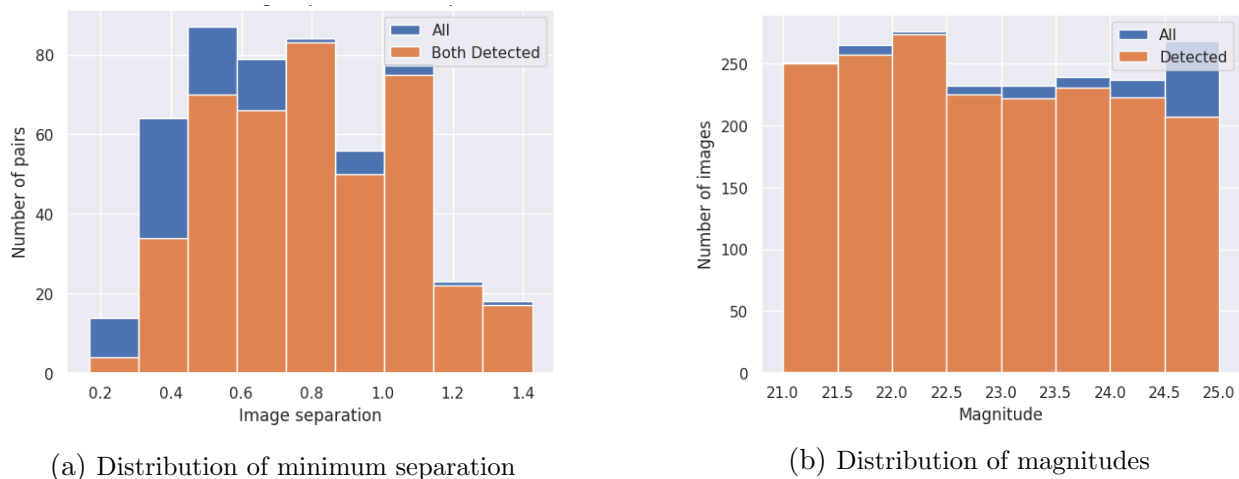
Figure 5.1: **Non lenses - separation and magnitude:** Fig (a) shows the distribution of the separation (in arcsec) for the closest pair of quasars in each image in blue. Overlaid in orange is the number of systems in which both the quasars were detected. Fig (b) shows the distribution of magnitudes of every *individual* quasar from all the images in blue and the distribution in orange counts all the individual quasars that have been detected.

had any effect on detection, we created a 2D histogram of minimum image separation and the difference in magnitude between the two quasars.

From Fig (5.2a) we can see that most images have a separation between 0.6 and 1.2 arcsec, and a difference in magnitude less than 1. We can see from Fig (5.2b) as well that the performance of the algorithm deteriorates below 0.5". The fraction of quads detected is also smaller for both higher(> 2.9) and lower (< 1) delta mag. If two quasars are close together in both position and magnitude space, then it becomes hard to say where one quasar ends and the other begins. If one of the quasars is much brighter than the other, then it will drown out the flux from the dimmer quasar making it hard to distinguish between the two of them again.

5.1.2   Mock Lenses

The position finder was run on 617 mock lensed quasars. In 419 images, all four quasars were successfully detected (within an error margin of 1.5 pixels), giving a success rate of $\sim 68\%$ In 4 of the systems, the program detected more than 4 peaks (i.e., 4 of the quasar peaks plus some extra peaks).

(a) 2D distribution plot of all images created

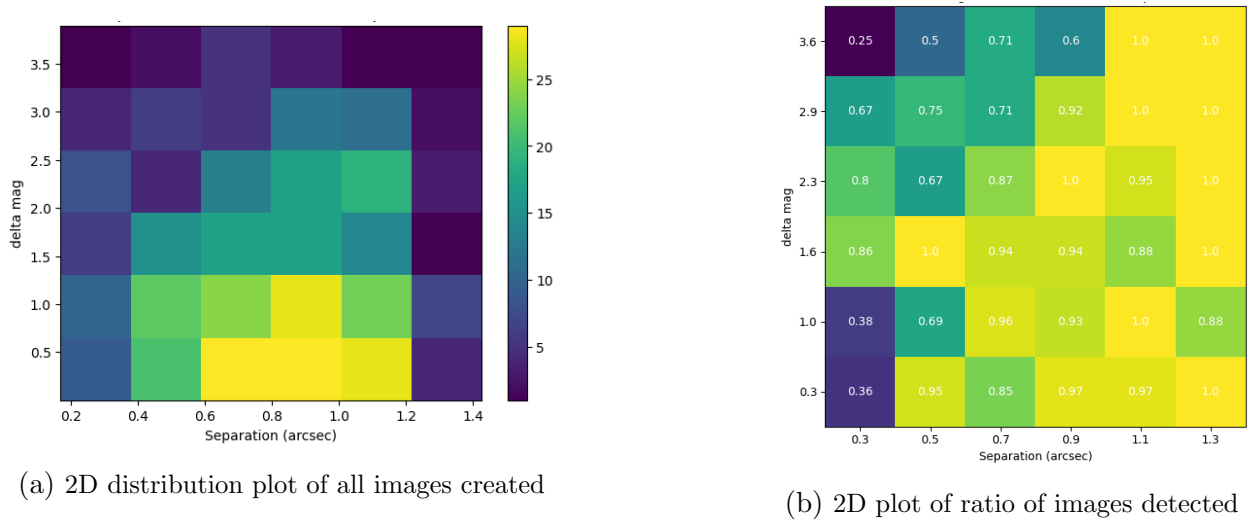(b) 2D plot of ratio of images detected

Figure 5.2: **Non-lenses-2D plots of separation and delta mag:** Fig (a) shows the 2D histogram between minimum image separation and difference in magnitudes of the two quasars in the pair with the smallest separation. The bins in this 2D histogram is populated with all the non-lens images created. Fig (b) shows for each bin of (a), the fraction of all the images where both the quasars of the pair have been detected.

The distribution of image separations in Fig (5.3a) shows nearly 100% success rate in detecting the closest pair of images until a separation of 0.6". There is a sharp drop in the rate of successful detection of both quasars in the closest pair below 0.5". We saw a similar trend with non-lenses as well. Fig (5.3b) shows the ratio of images where *all four* quasars were detected as a function of the closest image separation. This plot is nearly identical to Fig (5.3a) which indicates that the closest pairs are the ones not being detected in most of the cases where the algorithm has failed.

Fig 5.3c shows no clear trend in the fraction of total lenses detected for a given Einstein radius bin. There seems to be a small decrease in the fraction of lenses detected for smaller Einstein radii, which is expected. Our sample has a fairly narrow range of Einstein radii. The distribution of magnitudes (Fig 5.4) does not show any strong trends. Fig 5.4a shows a slight decrease in the fraction of lenses detected for higher magnitudes (fainter quasars). Overall, it seems like the performance of the position finder is not very affected by the magnitude of the quasar.

In lensed quasars, the closest pair of quasars usually have similar magnifications (and hence magnitudes). This can be seen in Fig 5.5a. There are no quasars in bins with larger delta mag. The fraction of detections again drops for separations less than 0.6". We also see

(a) Distribution of minimum separation - both detected

(b) Distribution of minimum separation - all detected
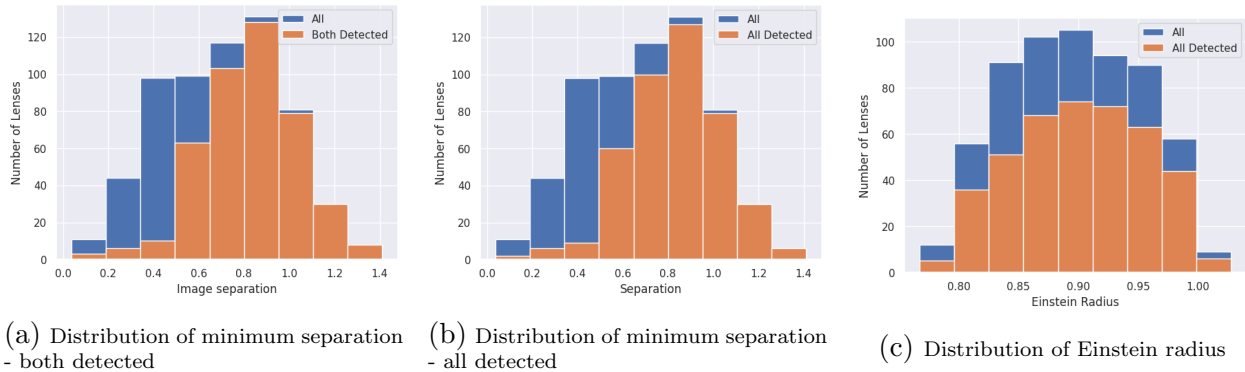
(c) Distribution of Einstein radius

Figure 5.3: **Mock lenses-image separation and Einstein radius:** Fig (a) shows the distribution of the separation (in arcsec) for the closest pair of quasars in each image in blue. Overlaid in orange is the number of systems in which both the quasars of the pair were detected. Fig (b) shows the same distribution as (a) in blue. For each separation bin, the orange histogram counts the total number of lenses where *all four* quasars were detected. Fig (c) plots the distribution of the Einstein radius of lenses in blue and the number of lenses where all four quasars were detected in orange.

that the bins with delta mag $= 0.3$ have, in general, a lower fraction of quads detected than bins above. The two bins with very large delta mag (2.6 and 3.2) that have been populated also have no detections. This is in line with the trend seen with non-lenses wherein very high and very low delta mag showed fewer detections.

The 2D histogram of minimum separation and magnitude of the fainter quasar in the closest pair (Fig 5.5b) shows that most quasars are concentrated between separation of $0.6" - 1.0"$ and magnitude of $19 - 21$. The fraction of detections for all separations (in Fig 5.5c) decreases as the quasars in the pair get fainter.

5.2   Schechter-Wynne Algorithm Tests

The Schechter-Wynne (SW) algorithm was first tested independent of the position finder to see if it is capable of differentiating between lenses and non-lenses. We used the actual positions used to create the mock lens and non-lens images and fed it into the SW algorithm. We used the results of these tests to decide the criteria based on which we will designate a system as a quadruply lensed quasar.

Out of the 500 non-lenses, 193 of them could not be modeled as an SIE potential. These can be immediately classified as non-lenses. Thus, we eliminated 39% of the non-lenses in

(a) Distribution of magnitudes-dimmest quasar
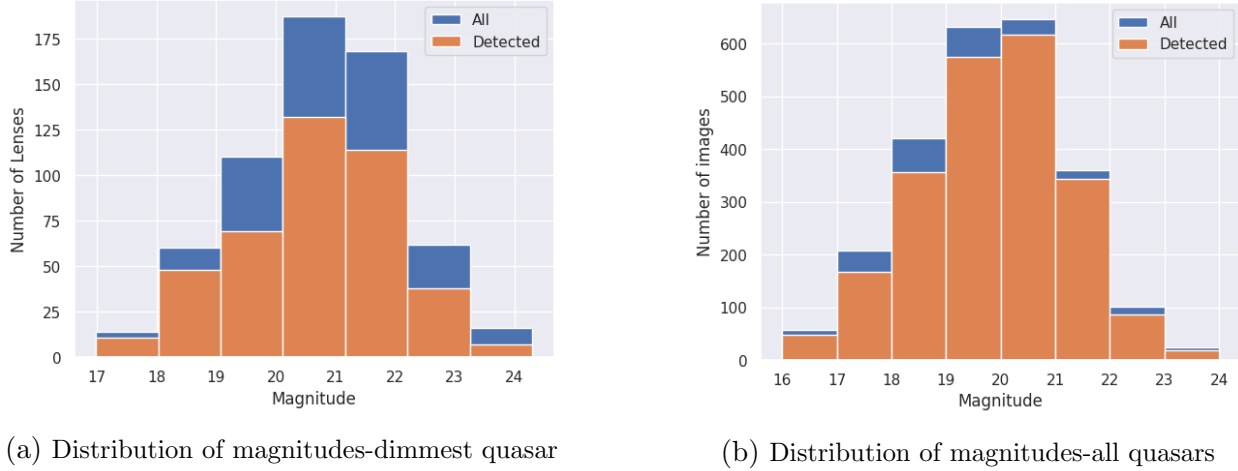
(b) Distribution of magnitudes-all quasars

Figure 5.4: **Mock lenses-distribution of magnitudes:** Fig (a) shows the distribution of magnitudes of the least bright quasar in each image, and the number of images that have been detected (i.e., where all quasars have been detected) for a particular magnitude bin. Fig (b) shows the distribution of magnitudes of all individual quasars and whether the quasar has been detected.
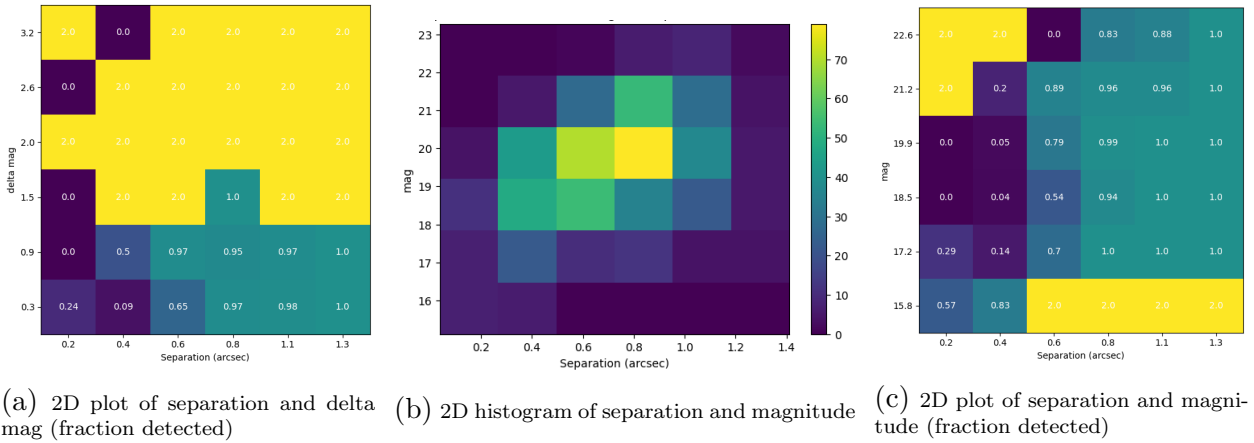

(a) 2D plot of separation and delta mag (fraction detected)

(b) 2D histogram of separation and magnitude

(c) 2D plot of separation and magnitude (fraction detected)

Figure 5.5: **Mock lenses-2D plots** Fig (a) shows the fraction of quads in which the closest pair has been detected as a function of separation between the two quasars and the difference between their magnitudes. The values of 2.0 (yellow) indicate that those bins were not populated. Fig (b) shows the number of quads created as a function of the minimum separation between two quasars in the quad and the magnitude of the fainter quasar in the pair with the smallest separation. Fig (c) shows the fraction of the quads detected in each of the bins of the previous histogram.
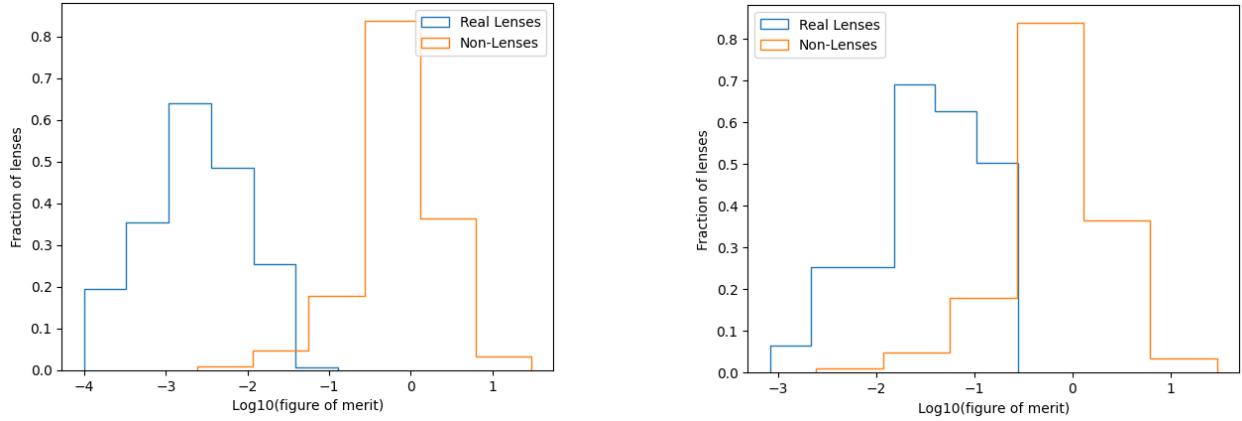
(a) Figure of merit - lenses and non-lenses

(b) Figure of merit - real lenses and non lenses

Figure 5.6: **Figure of merit - mock lenses, non lenses, and real lenses:** Fig (a) shows the normalised histogram of the log of figure of merit for 617 mock lenses and 307 non-lenses. The remaining 193 non-lenses could not be modeled as an SIE potential. Fig (b) shows the same for a sample of 38 real quadruply lensed quasars.

this step. The figure of merit for the remaining non-lenses is plotted in Fig 5.6.

The distribution of figure of merit(FoM) in Fig 5.6a shows good separation for lenses and non-lenses. But this is to be expected since the mock lenses are made using an SIE potential itself and we have used completely accurate positions of the quasars. To get a more realistic picture, I used the astrometry of 38 real lens systems that I had collected for Sec 3.3, and found the distribution of figure of merit (Fig 5.6b). If we accept all systems with log(FoM) less than -0.56, we can recover all the real lenses. Though we will then also accept around 16% of the remaining non-lenses plotted, which is 10% of all the non-lenses.

To understand how the distribution of the FoM for mock lenses will change when there is some error in the measurement of positions, we perturbed the true positions of the quasars in the mock lenses and used these perturbed positions to calculate the FoM histogram.

In the case when the position of one quasar in the image was perturbed by one pixel in either the x or y directions (Fig 5.7a), the limit of -0.56 on the log(FoM) will again give us a false positive rate of 10% and a false negative rate of less than 2%. Half of these false negatives consist of perturbed lenses that could not be modelled as an SIE potential. When three positions are perturbed (Fig 5.7b), a similar cutoff on log(FoM) will cause us to lose around 18.5% of lenses. Half of which, again, could not be modelled as SIEP. Increasing the value of log(FoM) to recover more lenses will drive up the false positive rate. Moving the

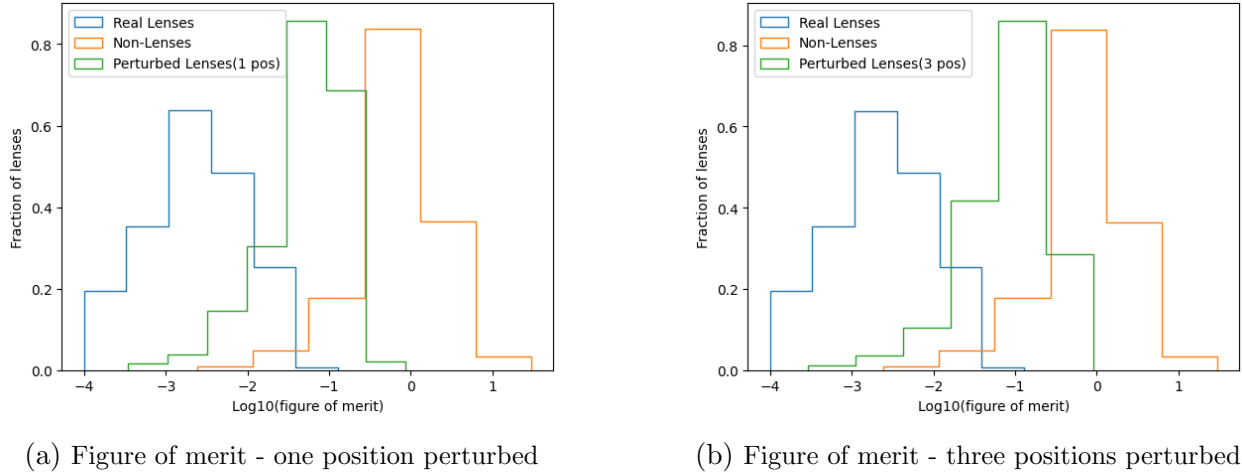(a) Figure of merit - one position perturbed

(b) Figure of merit - three positions perturbed

Figure 5.7: **Figure of merit - perturbed lenses:** Fig (a) shows the normalised histogram of the log(FoM) for mock lenses where the position of one of the quasars has been perturbed by one pixel (in x or y). log(FoM) for unperturbed lenses and non-lenses has also been plotted. Fig (b) shows the log(FoM) for mock lenses where positions of 3 quasars have been perturbed in either the x or y directions. Around 1% of the perturbed lenses are excluded from the plot in Fig(a) and around 9% from Fig(b) since they could not be modeled as an SIEP.

cutoff to -0.25 will improve the false negative rate to 10%, but the false positive rate will shoot up to over 20%.

To try and improve the rate of correct detection, we added the axis ratio of the amplitude ellipse as an additional variable that can be used to further differentiate between lenses and non-lenses. If we restrict the axis ratio $0.5 < q < 2$ with the same cutoff on log(FoM) of -0.56, then the false positive rate drops to 6.8% (Fig 5.8). In the case where one position of the quadruple system is perturbed, we lose 2 lenses. In the case where 3 positions are perturbed, we lose 16 lenses.

5.3   Combined Test

For the final test, we will see how well the two algorithms perform when working together. We used the positions of the quasars recovered using the Position-Finder to run the Schechter-Wynne algorithm and determined how well we are able to identify lensed quasars as opposed to random quadruple sources of light.

A cutoff of -0.56 on log(FoM) would allow us to recover around 91% of the mock lenses,

(a) FoM vs Axis Ratio - Mock Lenses

(b) FoM vs Axis Ratio - one position perturbed
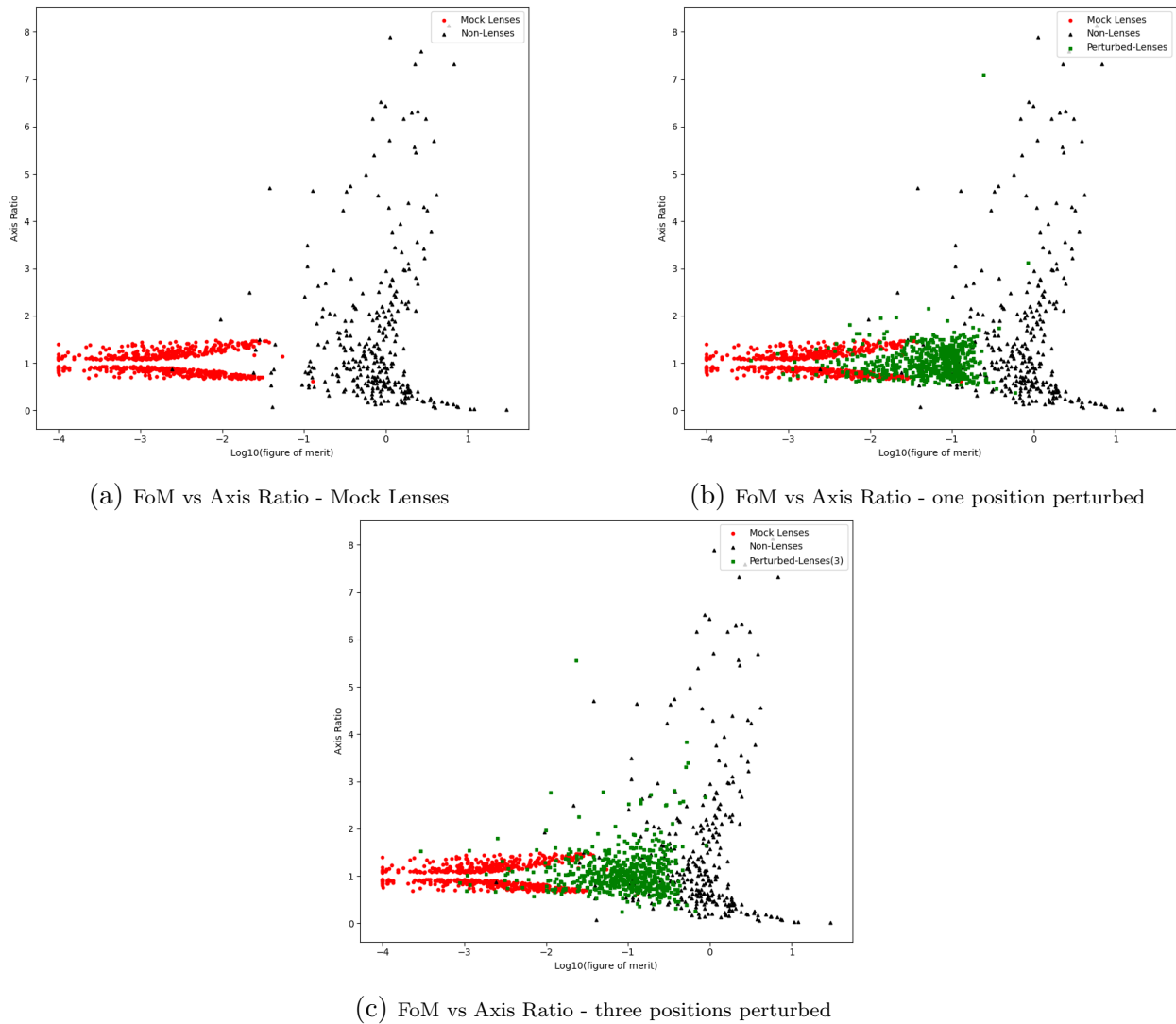

(c) FoM vs Axis Ratio - three positions perturbed

Figure 5.8: **Scatter plot - figure of merit and axis ratio:** Scatter plot of Log(FoM) vs axis ratio for lenses, non-lenses, and perturbed lenses. The axis ratio can be used as an additional parameter to differentiate between lenses and non-lenses, along with figure of merit.

with a 10% false positive rate (Fig 5.9a). Among the lenses that could not be identified, around 44 (7% of the total) of them could not be modelled by an SIE potential. If we further constrain the axis ratio, $0.5 < q < 2$, then we can reduce the false positive rate to 6.8% as shown before and we lose only 3 lenses (Fig 5.9b).

(a) Figure of merit - mock lenses and non-lenses

(b) Figure of merit vs axis ratio - lenses and non-lenses
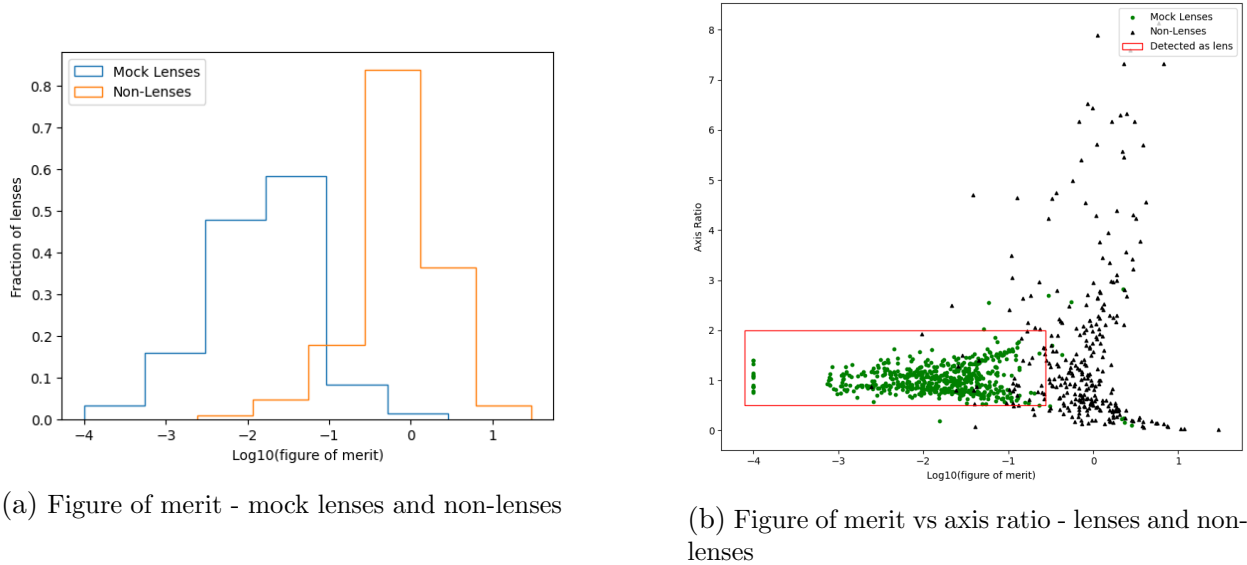
Figure 5.9: **Figure of merit-mock lenses combined test:** Figure of merit distribution for combined test of position finder and Schechter-Wynne algorithm using mock lenses. Fig (a) shows the normalised histogram of the log of figure of merit for mock lenses and non-lenses. Fig (b) also shows the axis ratio plotted on the y axis. The rectangular box contains all the mocks that fall within $log(FoM) < -0.56$ and $0.5 < q < 2$, and that are identified as lensed quasars by the program. The false positive rate of detection after restricting the axis ratio is 6.8%.

Given that the position finder was successful to very varying degrees based on the minimum separation of the quasars, it would be informative to study the rate of correct detection of lensed quasars by dividing them into two samples - *small separation* systems which consist of systems that have a minimum image separation less than 0.6". *Large separation* systems that consist of quasars with a minimum image separation greater than 0.6". Around 35% of the 617 mock lenses were small separation systems and the remaining 65% were large separation. In small separation systems, all four positions were correctly identified by position finder (upto an error of 1.5 pixels) with a success rate of 23%. And for large separation systems this number is $\sim 92\%$.
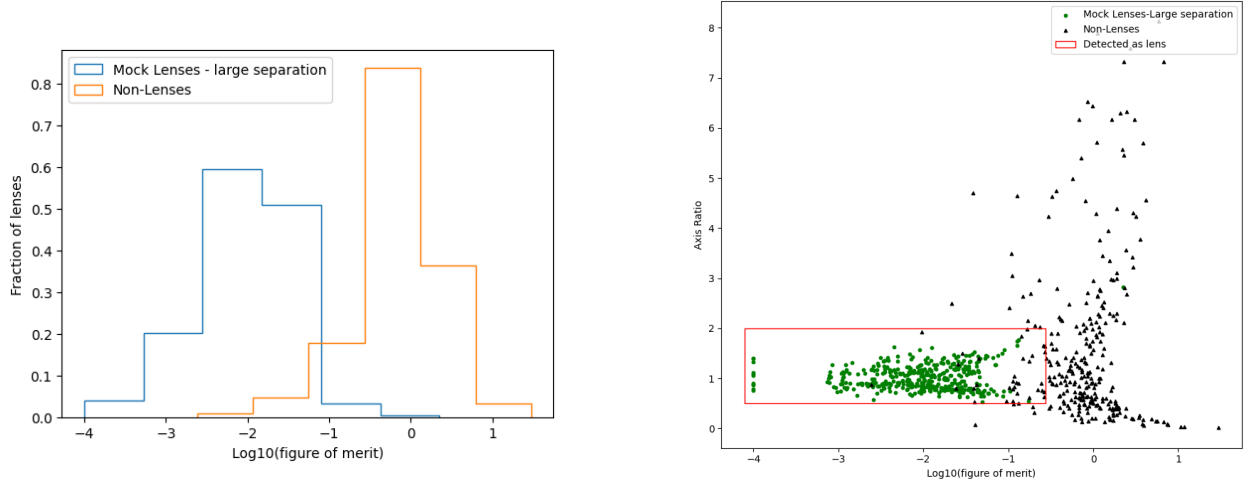
(a) Figure of merit - mock lenses and non-lenses

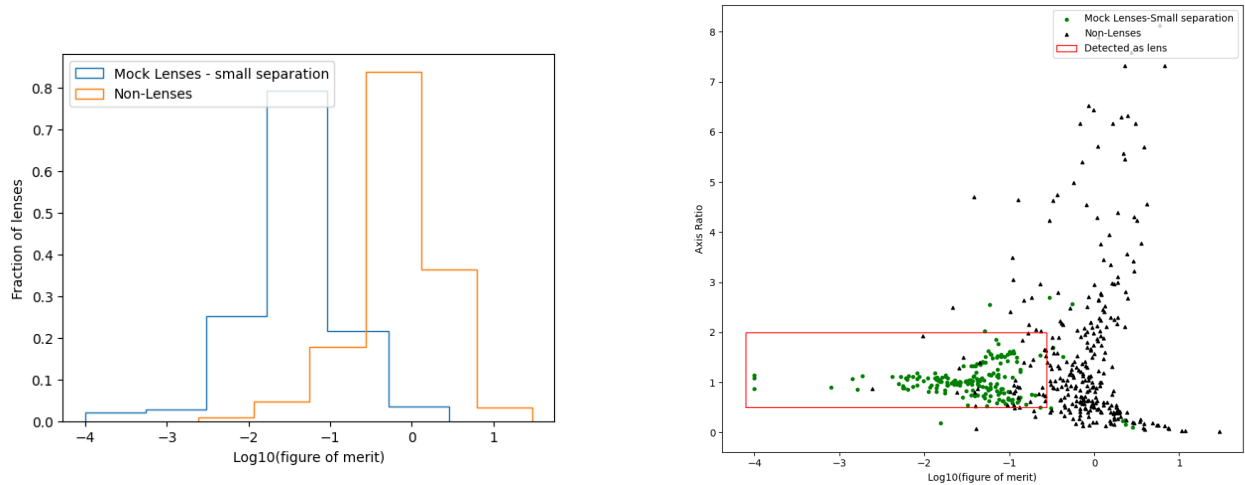(b) Figure of merit vs axis ratio - lenses and non-lenses

Figure 5.10: **Figure of merit: mock lenses with large separation combined test:** Figure of merit distribution for combined test of position finder and Schechter-Wynne algorithm using mock lenses with minimum image separation greater than 0.6". Fig (a) shows the normalised histogram of the log of figure of merit for mock lenses and non-lenses. We lose only 4.5% of the lenses and detect the rest. Fig (b) also shows the axis ratio plotted on the y axis. The rectangular box contains all the mocks that fall within $log(FoM) < -0.56$ and $0.5 < q < 2$, and that are identified as lensed quasars by the program.

5.3.1   Large separation quads

The program is able to identify lensed quasars with large image separations with a true positive rate of 95.5%. This is slightly higher than the accurate detection rate of position finder (92%). We can constrain the axis ratio (Fig 5.10) without losing any more quads. This gives a false positive rate of 6.8%.

5.3.2   Small separation quads

With small separation quads, we can see from Fig(5.11a) that the separation between lenses and non-lenses is worse than that for large separation quads. The true positive rate is around 83%. Three-quarters of the lenses not detected were unable to be modeled as an SIE potential (and hence not included in the histogram). After constraining the axis ratio (5.11b), we got a false positive rate of 6.8%, though we lost three more lenses in this process. A true positive rate of 83% is also very high given that the position finder was able to

(a) Figure of merit - mock lenses and non-lenses

(b) Figure of merit vs axis ratio - lenses and non-lenses

Figure 5.11: **Figure of merit-mock lenses with small separation combined test:** Figure of merit distribution for combined test of position finder and Schechter-Wynne algorithm using mock lenses with minimum image separation less than 0.6". Fig (a) shows the normalised histogram of the log of figure of merit for mock lenses and non-lenses. We lose $\sim 17\%$ of the lenses and detect the rest. Fig (b) also shows the axis ratio plotted on the y axis. The rectangular box contains all the mocks that fall within $log(FoM) < -0.56$ and $0.5 < q < 2$, and that are identified as lensed quasars by the program.

extract accurate positions with a success rate of only 23%. So it seems like for a significant population of lensed systems, even though the positions of the quasars were not entirely accurate, the systems still happen to fit an SIE potential quite well.

Chapter 6

Conclusion and Outlook

In this thesis project, we explored the fascinating world of gravitationally lensed quasars. In the first part of the project, we studied how quadruply-imaged quasar systems that have a highly asymmetric configuration of images point to the presence of a cluster or group of galaxies in the vicinity of the lens. The amount of "external shear" required to model these lenses could tell us if there is a cluster or group whose gravitational potential is contributing to the lensing. We calculated the distribution of external shear in a sample of quadruply lensed quasars that have been discovered and searched the literature on these lenses to see if groups had been identified in the immediate environment of lenses with large external shear. We found that in many cases, groups of galaxies had been found and in most cases, a search for a group/cluster that could be the reason for the large external shear was conducted. We were limited in our analysis by the small number of quadruply lensed quasars that have been discovered to date.

But this is expected to change in the near future. Upcoming telescopes like the Vera Rubin Observatory, Nancy Grace Roman, and Euclid space telescopes are going to discover thousands of strongly lensed quasars. An analysis such as the one described above could help us discover many more galaxy groups at intermediate redshifts which would aid galaxy evolution studies.

Our efforts in the second half of the thesis were focused on building an efficient automated lens hunter, which would be capable of sifting through terabytes of telescope image data and identifying quadruply lensed quasar candidates. We created a prototype of the program

during the thesis project and tested it on a set of mock lenses and non-lenses. The program consists of three major steps: Disentangling quasar and galaxy light from images, identifying quasar positions accurately, and fitting the Schechter-Wynne (SW) model to the positions of the quasars to determine if they belong to a lensed quasar system. The latter two steps were developed and tested on mocks based on the HSC-Wide survey images.

We divided the sample of mock lenses into two based on the minimum separation between two quasars in the images. Large separation systems had a minimum separation greater than 0.6" and small separation systems less than 0.6". The position finder had a success rate of 92% on large separation mocks and only 23% on small separation mocks, with a successful detection being defined as the detection of quasar position accurately up to an error of 1.5 pixels. Hence, the position finder seems to be effective only in detecting quasars with a minimum image separation larger than 0.6". But the SW algorithm was able to make up for the poor performance of the position finder, and we were able to recover around 83% of the lensed quasars with small separation. It was able to detect large separation mock lenses with a success rate of 95.5%. The overall true positive rate was around 91%. We tested the program on a sample of non-lens mocks as well, and it was able to differentiate between lenses and non-lenses fairly well. The false positive rate we obtained was close to 7%. We also tested the SW algorithm on a sample of 38 real quadruply lensed quasars. We were able to recover all 38 lenses and we accepted around 10% of the non-lenses.

Our test of the prototype program for detecting quadruply lensed quasar candidates shows promising results. But there is still a lot of work left to be done. Primarily, we need to develop and test the disentangling algorithm which is a necessary image-processing step that has to take place before any of the other algorithms can run. We will also have to test the program on a larger sample of mocks so that we can state the true and false positive rates with more certainty. Since our aim is to create a program that is fast as well as accurate, we need to quantify the speed of classifying images as lenses or non-lenses. Finally, we hope to be able to run this program on data from the HSC-Wide survey to search for new quadruply-lensed quasar candidates.

Given the large amounts of data that current and future telescopes are going to produce, it is important that we have efficient automated methods of identifying lensed quasar candidates. Our program, once completed, can be a valuable addition to the host of strong lensing detection methods that exist today.

Bibliography

[1] Adriano Agnello et al. "Data mining for gravitationally lensed quasars". In: *Monthly Notices of the Royal Astronomical Society* 448 (2 Apr. 2015), pp. 1446–1462. ISSN: 1365-2966. DOI: 10.1093/mnras/stv037.

[2] C. T. Berghea et al. "Discovery of the First Quadruple Gravitationally Lensed Quasar Candidate with Pan-STARRS". In: 844.2, 90 (Aug. 2017), p. 90. DOI: 10.3847/1538-4357/aa7aa6. arXiv: 1705.08359 [astro-ph.GA].

[3] Daniela Bettoni et al. "A New Einstein Cross Gravitational Lens of a Lyman-break Galaxy". In: 873.2, L14 (Mar. 2019), p. L14. DOI: 10.3847/2041-8213/ab0aeb. arXiv: 1902.10964 [astro-ph.GA].

[4] S. Birrer et al. "Time-Delay Cosmography: Measuring the Hubble Constant and other cosmological parameters with strong gravitational lensing". In: *arXiv e-prints*, arXiv:2210.10833 (Oct. 2022), arXiv:2210.10833. DOI: 10.48550/arXiv.2210.10833. arXiv: 2210.10833 [astro-ph.CO].

[5] Adam S. Bolton et al. "The Sloan Lens ACS Survey. I. A Large Spectroscopically Selected Sample of Massive Early-Type Lens Galaxies". In: *The Astrophysical Journal* 638 (2 Feb. 2006), pp. 703–724. ISSN: 0004-637X. DOI: 10.1086/498884.

[6] V. Bonvin et al. "H0LiCOW – V. New COSMOGRAIL time delays of HE 04351223: H0 to 3.8 per cent precision from strong lensing in a flat CDM model". In: *Monthly Notices of the Royal Astronomical Society* 465.4 (Nov. 2016), pp. 4914–4930. ISSN: 0035-8711. DOI: 10.1093/mnras/stw3006. eprint: https://academic.oup.com/mnras/article-pdf/465/4/4914/10254866/stw3006.pdf.

[7]   James H.H. Chan et al. "Chitah: STRONG-GRAVITATIONAL-LENS HUNTER in IMAGING SURVEYS". In: *Astrophysical Journal* 807 (2 July 2015). ISSN: 15384357. DOI: 10.1088/0004-637X/807/2/138.

[8]   Dani C.-Y. Chao et al. "Lensed quasar search via time variability with the HSC transient survey". In: *Astronomy Astrophysics* 640 (Aug. 2020), A88. ISSN: 0004-6361. DOI: 10.1051/0004-6361/201936806.

[9]   S. Ertl et al. "TDCOSMO XI. Automated Modeling of 9 Strongly Lensed Quasars and Comparison Between Lens Modeling Software". In: *arXiv e-prints*, arXiv:2209.03094 (Sept. 2022), arXiv:2209.03094. arXiv: 2209.03094 [astro-ph.CO].

[10] E. E. Falco, M. V. Gorenstein, and I. I. Shapiro. "On model-dependent bounds on H 0 from gravitational images : application to Q 0957+561 A, B." In: 289 (Feb. 1985), pp. L1–L4. DOI: 10.1086/184422.

[11] Gilbert P. Holder and Paul L. Schechter. "External Shear in Quadruply Imaged Lens Systems". In: *The Astrophysical Journal* 589 (2 June 2003), pp. 688–692. ISSN: 0004-637X. DOI: 10.1086/374688.

[12] Aggeliki Kassiola and Israel Kovner. "Elliptic Mass Distributions versus Elliptic Potentials in Gravitational Lenses". In: 417 (Nov. 1993), p. 450. DOI: 10.1086/173325.

[13] Charles R. Keeton and Leonidas A. Moustakas. "A NEW CHANNEL FOR DETECTING DARK MATTER SUBSTRUCTURE IN GALAXIES: GRAVITATIONAL LENS TIME DELAYS". In: *The Astrophysical Journal* 699 (2 July 2009), pp. 1720–1731. ISSN: 0004-637X. DOI: 10.1088/0004-637X/699/2/1720.

[14] C. S. Kochanek. "Strong Gravitational Lensing". In: *Gravitational Lensing: Strong, Weak and Micro*. Berlin, Heidelberg: Springer Berlin Heidelberg, 2006, pp. 91–268. ISBN: 978-3-540-30310-7. DOI: 10.1007/978-3-540-30310-7_2.

[15] C. Lemon et al. "Gravitationally lensed quasars in Gaia – IV. 150 new lenses, quasar pairs, and projected quasars". In: *arXiv e-prints*, arXiv:2206.07714 (June 2022), arXiv:2206.07714. arXiv: 2206.07714 [astro-ph.GA].

[16] C. Lemon et al. "The STRong lensing Insights into the Dark Energy Survey (STRIDES) 2017/2018 follow-up campaign: discovery of 10 lensed quasars and 10 quasar pairs". In: 494.3 (May 2020), pp. 3491–3511. DOI: 10.1093/mnras/staa652. arXiv: 1912.09133 [astro-ph.GA].

[17] Cameron A Lemon, Matthew W Auger, and Richard G McMahon. "Gravitationally lensed quasars in ¡i¿Gaia¡/i¿ – III. 22 new lensed quasars from ¡i¿Gaia¡/i¿ data release 2". In: *Monthly Notices of the Royal Astronomical Society* 483 (3 Mar. 2019), pp. 4242–4258. ISSN: 0035-8711. DOI: 10.1093/mnras/sty3366.

[18] Philip J. Marshall et al. "AUTOMATED DETECTION OF GALAXY-SCALE GRAV-ITATIONAL LENSES IN HIGH-RESOLUTION IMAGING DATA". In: *The Astro-physical Journal* 694 (2 Apr. 2009), pp. 924–942. ISSN: 0004-637X. DOI: 10.1088/0004-637X/694/2/924.

[19] Leonidas A. Moustakas et al. "Strong gravitational lensing probes of the particle na-ture of dark matter". In: *astro2010: The Astronomy and Astrophysics Decadal Survey*. Vol. 2010. Jan. 2009, p. 214. DOI: 10.48550/arXiv.0902.3219. arXiv: 0902.3219 [astro-ph.CO].

[20] S. T. Myers et al. "The Cosmic Lens All-Sky Survey - I. Source selection and obser-vations". In: *Monthly Notices of the Royal Astronomical Society* 341 (1 May 2003), pp. 1–12. ISSN: 00358711. DOI: 10.1046/j.1365-8711.2003.06256.x.

[21] Ramesh Narayan and Matthias Bartelmann. "Lectures on Gravitational Lensing". In: *arXiv e-prints*, astro-ph/9606001 (June 1996), astro–ph/9606001. arXiv: astro-ph/9606001 [astro-ph].

[22] Ramesh Narayan and Matthias Bartelmann. "Lectures on Gravitational Lensing". In: *arXiv e-prints*, astro-ph/9606001 (June 1996), astro–ph/9606001. DOI: 10.48550/arXiv.astro-ph/9606001. arXiv: astro-ph/9606001 [astro-ph].

[23] Masamune Oguri. "The Mass Distribution of SDSS J1004+4112 Revisited". In: 62 (Aug. 2010), p. 1017. DOI: 10.1093/pasj/62.4.1017. arXiv: 1005.3103 [astro-ph.CO].

[24] Masamune Oguri et al. "The Sloan Digital Sky Survey Quasar Lens Search. I. Candi-date Selection Algorithm". In: *The Astronomical Journal* 132 (3 Sept. 2006), pp. 999–1013. ISSN: 0004-6256. DOI: 10.1086/506019.

[25] Somak Raychaudhury, Prasenjit Saha, and Liliya L. R. Williams. "Is B1422+231 a "Golden Lens"?" In: *The Astronomical Journal* 126 (1 July 2003), pp. 29–36. ISSN: 0004-6256. DOI: 10.1086/375326.

[26] Cristian E Rusu et al. "A search for gravitationally lensed quasars and quasar pairs in Pan-STARRS1: spectroscopy and sources of shear in the diamond 2M11342103". In: *Monthly Notices of the Royal Astronomical Society* 486 (4 July 2019), pp. 4987–5007. ISSN: 0035-8711. DOI: 10.1093/mnras/stz1142.

[27] Prasenjit Saha and Liliya L. R. Williams. "Qualitative Theory for Lensed QSOs". In: 125.6 (June 2003), pp. 2769–2782. DOI: 10.1086/375204. arXiv: astro-ph/0303261 [astro-ph].

[28] Prasenjit Saha and Liliya L. R. Williams. *SimpLens: Interactive gravitational lensing simulator*. Astrophysics Source Code Library, record ascl:1606.010. June 2016. ascl: 1606.010.

[29] Paul L. Schechter and Raymond A. Wynne. "Even Simpler Modeling of Quadruply Lensed Quasars (and Random Quartets) Using Witt's Hyperbola". In: *The Astrophysical Journal* 876 (1 Apr. 2019), p. 9. ISSN: 15384357. DOI: 10.3847/1538-4357/ab1258.

[30] T. Schmidt et al. "STRIDES: Automated uniform models for 30 quadruply imaged quasars". In: *arXiv e-prints*, arXiv:2206.04696 (June 2022), arXiv:2206.04696. arXiv: 2206.04696 [astro-ph.CO].

[31] P. Schneider. "Introduction to Gravitational Lensing and Cosmology". In: *Gravitational Lensing: Strong, Weak and Micro*. Berlin, Heidelberg: Springer Berlin Heidelberg, 2006, pp. 1–89. ISBN: 978-3-540-30310-7. DOI: 10.1007/978-3-540-30310-7_1.

[32] Peter Schneider, Jürgen Ehlers, and Emilio E. Falco. "Derivation of the lens equation". In: *Gravitational Lenses*. Berlin, Heidelberg: Springer Berlin Heidelberg, 1992, pp. 119–155. ISBN: 978-3-662-03758-4. DOI: 10.1007/978-3-662-03758-4_4.

[33] Peter Schneider, Jürgen Ehlers, and Emilio E. Falco. *Gravitational Lenses*. 1992. DOI: 10.1007/978-3-662-03758-4.

[34] Peter Schneider, Jürgen Ehlers, and Emilio E. Falco. "Optics in curved spacetime". In: *Gravitational Lenses*. Berlin, Heidelberg: Springer Berlin Heidelberg, 1992, pp. 91–117. ISBN: 978-3-662-03758-4. DOI: 10.1007/978-3-662-03758-4_3.

[35] Peter Schneider, Jürgen Ehlers, and Emilio E. Falco. "Properties of the lens mapping". In: *Gravitational Lenses*. Berlin, Heidelberg: Springer Berlin Heidelberg, 1992, pp. 157–181. ISBN: 978-3-662-03758-4. DOI: 10.1007/978-3-662-03758-4_5.

[36] A. J. Shajib et al. "Is every strong lens model unhappy in its own way? Uniform modelling of a sample of 13 quadruply+ imaged quasars". In: (July 2018). DOI: 10. 1093/mnras/sty3397.

[37] A. J. Shajib et al. "STRIDES: a 3.9 per cent measurement of the Hubble constant from the strong lens system DES J0408-5354". In: 494.4 (June 2020), pp. 6072–6102. DOI: 10.1093/mnras/staa828. arXiv: 1910.06306 [astro-ph.CO].

[38] A. J. Shajib et al. "Strong Lensing by Galaxies". In: (Oct. 2022). URL: http://arxiv. org/abs/2210.10790.

[39] D. Stern et al. "Gaia GraL: Gaia DR2 Gravitational Lens Systems. VI. Spectroscopic Confirmation and Modeling of Quadruply Imaged Lensed Quasars". In: 921.1, 42 (Nov. 2021), p. 42. DOI: 10.3847/1538-4357/ac0f04. arXiv: 2012.10051 [astro-ph.GA].

[40] S. Vegetti et al. "Gravitational detection of a low-mass dark satellite galaxy at cosmological distance". In: *Nature* 481 (7381 Jan. 2012), pp. 341–343. ISSN: 0028-0836. DOI: 10.1038/nature10669.

[41] Hans J. Witt. "Using Quadruple Lenses to Probe the Structure of the Lensing Galaxy". In: 472 (Nov. 1996), p. L1. DOI: 10.1086/310358. arXiv: astro-ph/9608197 [astro-ph].

[42] Raymond A. Wynne and Paul L. Schechter. "Robust modeling of quadruply lensed quasars (and random quartets) using Witt's hyperbola". In: *arXiv: Cosmology and Nongalactic Astrophysics* (2018).